

POSTGRADUATE ENVIRONMENTAL PHYSICS
DEPARTMENT OF CLIMATE MODELLING

Understanding dependency structures in major modes of climate variability with causal discovery

Master Thesis

Supervisor/Examiner: Prof. Dr. Veronika Eyring

Second Examiner: Prof. Dr. Thomas Jung

Second Supervisor: Dr. Jakob Runge

SOUFIANE KARMOUCHE

Date of birth: **30/07/1993**

Matriculation number: **3121381**

To be submitted before: **January, 24th 2020**



ABSTRACT

Accurate climate change projections depend on the ability of climate models to correctly represent major modes of climate variability and large-scale teleconnections. However, the evaluation of modes of variability is to date largely based on means, climatologies, or spectral properties which cannot always reveal whether a climate model correctly simulates the dynamical dependencies between different climatological processes or lagged long-distance teleconnections. The goal of this Master thesis is to construct causal interdependency networks for the major modes of variability from models participating in the Coupled Model Intercomparison Project Phase 6 (CMIP6). This is done by applying an existing novel algorithm for causal discovery to construct causal networks for the major modes of variability from models and reanalysis data and are compared, thus going beyond simple descriptive statistics of the model output. In addition, changes in dependency structures are analysed for different future scenarios. The Tigramite python package uses time series as input data and reconstructs a causal graph. The latter is a special kind of graphical model that translates the conditional dependency structures of the selected components at different time lags. The input time series data are generated using the NCAR Climate Variability Diagnostics Package (CVDP) within the Earth System Model Evaluation Tool (ESMValTool). The ESMValTool is a community diagnostics and performance metrics tool for the evaluation of Earth System Models (ESMs). For the resulting time series of the major modes of climate variability, a graphical model is constructed that encodes the link strength by which climate variability indices and certain atmospheric or ocean variables (sea surface temperature, sea level pressure, precipitation) are interconnected to modes of climate variability. The graphical model also provides the time lag by which the detected causality is effective. First, the method is used for CMIP6 data to reconstruct two climate examples that have previously been applied to reanalyses data. They illustrate teleconnections between surface-air temperatures (TAS) over Eastern and Western Europe, in addition to the interplay between sea level pressure (PSL) anomalies over the Western Pacific and TAS anomalies over both the Central and Eastern Pacific. Performance of recreating the same results as the NCEP-NCAR reanalysis dataset is found to vary from one model to the other. Nonetheless, the multi-model mean (averaging 6 CMIP6 models) reproduces all links created by the reference dataset with similar time lags. Second, the algorithm is used to analyse the interplay between El Niño-Southern Oscillation (ENSO) and four other major modes of climate variability: the Pacific Decadal Oscillation (PDO), the Pacific North American pattern (PNA), the Indian Ocean Dipole (IOD), and the North Atlantic Oscillation (NAO). The idea is to study the basin-wide teleconnections involving these modes over the Pacific Ocean, the Indian Ocean, and the North Atlantic Ocean. Here, a regime-oriented analysis is applied to show how the basin-wide

ENSO connections decay when PDO and ENSO are out of phase. Based on comparison with the reference reanalysis dataset, most of the models reproduce the well-established strong connection between PDO and PNA, and the negatively correlated PNA—NAO connection for historical and pre-industrial control simulations. Results also show that the causal network changes according to different future scenarios. Not only connections are found to weaken but also the overall number of connections is found to drop significantly when moving from a moderate radiative forcing scenario to a high radiative forcing scenario.

Table of Contents

1. INTRODUCTION	6
2. SCIENTIFIC BASIS: Modes of variability and their dependency structures	8
2.1. Physical basis for internal climate variability	8
2.2. Well-known dependencies between selected modes of variability	13
3. DATA	15
3.1. Climate model simulations	15
3.2. Reanalysis data for model evaluation	16
4. METHODS	17
4.1. NCAR Climate Variability Diagnostics Package (CVDP)	17
4.2. ESMValTool	19
4.3. Tigramite for Causality detection: PCMCI	20
5. RESULTS	22
5.1. Reconstruction of climate examples	22
5.2. Regime-oriented causal discovery	26
6. DISCUSSION	35
7. CONCLUSIONS	37
8. REFERENCES	39
9. APPENDIX:	46
LIST OF FIGURES:	52
LIST OF TABLES:	53

1. INTRODUCTION

Climate variability is defined by the variations in the mean state of climate or its statistical aspects (e.g. standard deviations) on all spatio-temporal scales beyond that of individual weather events (Selvaraju, 2007). Generally, climate variability is a result of either natural processes generated internally in the climate system or in response to natural external forcing. Climate variability, hence, can result from two sources: First, internal Climate variability from interactions between different components of the climate system such as the processes between land and atmosphere or most importantly those between ocean and atmosphere, and second, natural external forcing; for example, volcanoes or the number of sunspots and how it changes the amount of solar radiation received by Earth. In addition to natural forcers, anthropogenic activities such as the emission of greenhouse gases from burning of fossil fuels lead to climate change (IPCC, 2013). Timescales for the modes of climate variability originating from internal climate variability vary from seasons, to years, to decades or even to millennia.

Climate models are able to simulate both types of climate variability. In order to test their realism, the models are compared to observations or reanalysis data. However, through the various previous Coupled Model Intercomparison Project (CMIP) phases, comparisons with observations have often revealed systematic errors in large multi-model ensembles; errors that have only little or no improvement (Stouffer et al., 2017). Examples of these systematic errors are the dry Amazon bias, or differences in the magnitude and frequency of the El Niño-Southern Oscillation (ENSO) (Flato et al., 2014; Randall et al., 2007). Because of the complexity of the climate system, it is difficult to assign a specific cause to a specific systematic error (bias). Modes of natural climate variability from interannual to multi-decadal time scales are important as they have large impacts on regional and even global climate with attendant socio-economic impacts. These modes are emergent and spontaneously occurring phenomena and need not exhibit the same chronological sequence in models as in nature. Their statistical properties (e.g., time scale, autocorrelation, spectral characteristics, and spatial patterns) however should be captured by climate models. Despite their importance, systematic evaluation of these modes remains a daunting task given the wide range to consider, the length of the data record needed to adequately characterize them, the importance of sub-surface oceanic processes and uncertainties in the observational records (Eyring et al., 2019b).

Evaluation of the major modes of variability is to date largely based on means, climatologies, or spectral properties (Deser et al., 2010; Phillips et al., 2014) which cannot always reveal whether a climate model correctly simulates the dynamical mechanisms between different climatological

processes, for example the interplay between ENSO and the Pacific Decadal Oscillation (Steinhaeuser and Tsonis, 2014) or lagged long-distance teleconnections. It is therefore a priority to find new approaches for evaluating climate models in an efficient way that reveals linkages between geographical regions or time intervals and uncovers the relevant processes. The paradigm of causal discovery provides methods to estimate such dynamical dependencies from data time series (Fountalis et al., 2015; Runge et al., 2019; Runge et al., 2015; Steinhaeuser and Tsonis, 2014) and can help to understand whether a model simulates specific phenomena for the right reasons.

The goal of this Master thesis is to construct causal interdependency networks for the major modes of variability from models and observations and to compare them, thus going beyond the simple descriptive statistics of the model output. To do so, an existing algorithm for advanced methods on causal discovery (Runge et al., 2015) is used to analyse models participating in the Coupled Model Intercomparison Project Phase 6 (Eyring et al., 2016a).

The algorithm is called PCMCI, which stands for Peter Clark Momentary Conditional Independence and which is implemented on the Tigramite python package. Tigramite with its detailed documentation can be found under: <https://jakobrunge.github.io/tigramite/> Tigramite “allows to efficiently reconstruct causal graphs from high-dimensional time series datasets and model the obtained causal dependencies for causal mediation and prediction analyses” (Runge et al., 2017).

The Master thesis is structured as follows. Section 2 describes the physical mechanisms why climate variability and different modes of variability occur. In Section 3, the observation reference datasets and the models used in this thesis are presented. Section 4 introduces the different tools used for the analysis. Section 5.1 first explains the methodology by reconstructing benchmark examples from Runge et al. (2014) before introducing the focus of this thesis: the regime-oriented analysis on the selected major modes of climate variability in Section 5.2. A discussion and conclusions are presented in Section 6 and 7, respectively.

2. SCIENTIFIC BASIS: Modes of variability and their dependency structures

2.1. Physical basis for internal climate variability

Climate, describing the long-term trends of weather, is affected by the interactions between the atmosphere and the ocean, the land, the biosphere, and the cryosphere. Mass, energy and momentum are exchanged between these Earth system components resulting in regular fluctuations in the climate variables (e.g., sea surface temperature (SST) , surface sea level pressure (SLP)) on regional and global scales. Fluctuations in the mean state of climate on all time scales is a natural form of climate variability. The modes of climate variability, i.e. oscillations, represent these regular fluctuations on regional scales (de Viron et al., 2013). Figure 1 by Deser et al. (2010) shows the example of slow SST variations that may be brought by random (usually unpredictable) atmospheric forcing. The figure presents a stochastic climate model paradigm by illustrating the response of the mixed-layer temperature to randomly varying surface heat flux for two different ocean depths (shallow at 50 m, and deep at 500 m). It is shown that SST fluctuates on the order of a couple of years at the shallow (50 m) layer, compared to the order of decades by which SST oscillates at the deep (500 m) layer. When describing his stochastic climate model, Hasselmann (1976) divides the Earth System into a rapidly varying “weather” system (mainly the atmosphere) and a slowly responding “climate” system (the ocean, cryosphere, land vegetation, etc.). This discrepancy is responsible for climate variability and is manifested through the ocean integration of atmospheric noise. The atmosphere is considered as white noise, whereas the ocean, with its much higher heat capacity, plays the role of a low-pass filter (especially at midlatitudes). This generally generates SST-anomaly feedbacks at the mixed layer with a characteristic feedback time in the order of 6 months maximum (Frankignoul and Hasselmann, 1977). For a truly coupled atmosphere-ocean mode to happen, atmospheric heat and momentum fluxes have to be induced by oceanic SST in order to strengthen it (Anderson and Willebrand, 2013). Studies by Lau and Nath (1994) and Graham et al. (1994) suggest that the effects on the atmosphere over midlatitude SST is dominated by tropical SST. This is essentially why tropical modes are found to be more coupled than midlatitude modes. In their book about the dynamics and predictability of decadal climate variability, Anderson and Willebrand (2013) explain that “most higher latitude modes require higher latitude SST to affect the atmosphere”; an influence that has been difficult to detect. The structure of these modes is generally fixed by the continents and ocean basins.

Oceans provide a large source of thermal inertia to the atmosphere. They translate this thermal inertia to the overlying atmosphere mainly through turbulent fluxes of sensible and latent heat at the surface. These surface turbulent fluxes depend on SSTs in addition to the various atmospheric parameters (e.g., near-surface wind speed, air temperature, relative humidity) (Deser et al., 2003).

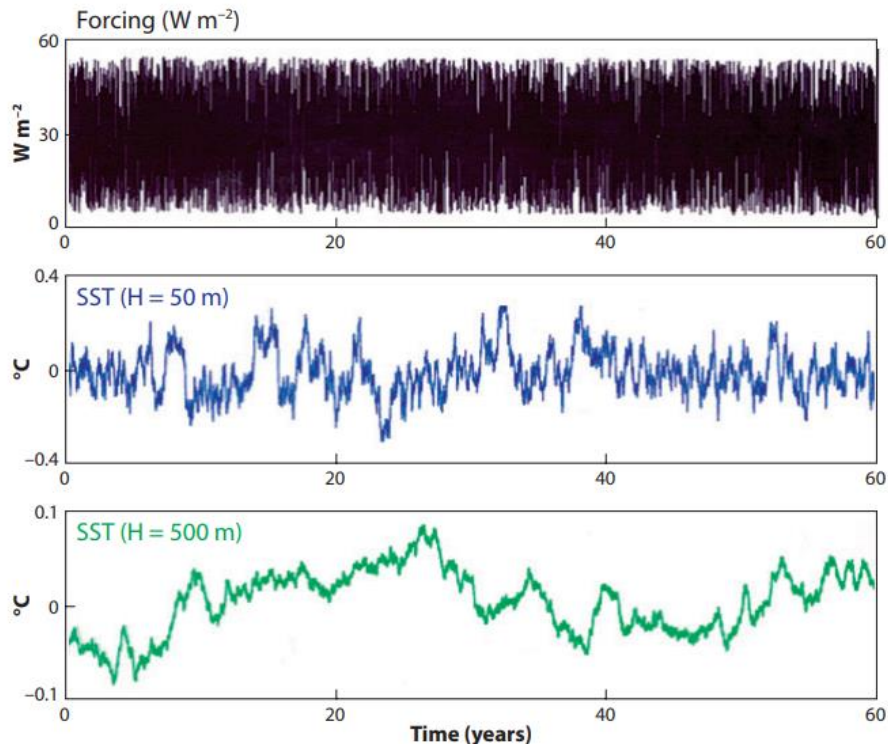


Figure 1. Random atmospheric heat flux forcing time series (top) and the upper-ocean mixed-layer temperature response for a mixed-layer depth of 50 m (middle) and 500 m (graph). (Deser et al., 2010)

An important research question is how modes of climate variability impact (and/or are impacted by) one another. The focus for this thesis is on tropical and extra-tropical dependencies of major modes of climate variability in the Pacific, the Indian and the North Atlantic Oceans. This is done by constructing a causal network from time series of: ENSO, the Indian Ocean Dipole (IOD), the Pacific North American (PNA) pattern, the Pacific Decadal Oscillation (PDO) and the North Atlantic Oscillation (NAO). A table summarizing how the indices of these modes are calculated is presented in section 4.1 (Table 2)

El Niño - Southern Oscillation (ENSO), originating from the tropical Pacific, has significant ecological effects for example on natural habitats and fisheries in this region (Timmermann et al., 1999). Moreover, it influences the global climate system through a wide network of teleconnection patterns, resulting in socio-economic impacts on many countries around the world (Glantz et al., 1991). ENSO refers to the coupled SST anomalies and SLP fluctuations over the tropical Pacific Ocean (Graham et al., 2015). ENSO is the world's most prominent mode of climate variability. This interannual mode is generated through air-ocean interactions over the tropical Pacific and

alternates between anomalously warm (El Niño) and anomalously cold (La Niña) SSTs. A schematic illustrating the oceanic and weather conditions during normal conditions, El Niño and La Niña is shown in Figure 2. During El Niño, the easterly trade winds weaken due to the formation of a higher surface air pressure system over the western Pacific compared to the pressure system over the tropical east Pacific (Bjerknes, 1969). The weakened trade winds and zonal currents act as a barrier to ocean upwelling, resulting in a deeper-than-normal thermocline and higher SSTs over the central and eastern tropical parts of the Pacific. The usual precipitation pattern is also shifted further to the east than its normal position. In contrast to El Niño conditions, La Niña knows stronger-than-normal trade winds in the Tropical Pacific increasing the upwelling rate over the equator and along the west coast of South America. The SSTs over eastern Pacific are then colder than normal. The main precipitation pattern is shifted further west during la Niña (Yeh et al., 2018).

In addition to ENSO's basin-wide signal through fast atmospheric Walker circulation (Klein et al., 1999), the Indian Ocean (IO) generates its own mode of climate variability; the Indian Ocean Dipole (IOD). IOD, identified as a mode of climate variability in 1999, is generated through air-sea coupling in the tropical IO and denotes SST oscillations creating temperature gradients between western and eastern IO (Saji et al., 1999). Along the southeast region of the equatorial Indian Ocean, positive IOD can be illustrated through negative SST anomalies. On the other hand, western IO experiences weak positive anomalies. In contrast, IOD can also reversely, during its negative phase, denote positive SST anomalies in the southeast, coupled with negative anomalies along the west (Zheng et al., 2013).

The PNA exemplifies the quadripole anomaly field of 500 hPa geopotential height (H_{500}) with anomalies of similar sign over the region south of Aleutian Islands and the region over southeastern United States. The region over the vicinity of Hawaii, and the north-western-North American region (central Canada) know opposite sign anomalies to that of the Aleutian centre. During the positive phase of PNA, there are above normal H_{500} over western U.S. and below normal H_{500} over eastern U.S. and vice versa (Leathers et al., 1991; Wallace and Gutzler, 1981).

The PDO is the dominant decadal variability in the North Pacific. It is responsible for anomalies of Northern Hemisphere climate as well as North Pacific ecosystems (Mantua et al., 1997). Its temporal evolution is characterized by an interannual and decadal variability with some pronounced shifts, notably the extensively studied 1976/77 transition. Biologists reported dramatic changes in the biota over the North Pacific during the late 1970's regime shift. Ebbesmeyer et al. (1991) identified changes in 40 climatic and biological variables with a statistically significant

step during that period. PDO is often seen as a long-lived El Niño-like pattern over the North Pacific. Like ENSO, it fluctuates from positive and negative phases. The warm (positive) PDO phase is when the central North Pacific knows anomalously cool SSTs while SSTs along the Pacific Coast are anomalously warm. When these climate patterns reverse, the PDO is in its negative phase; i.e. warm SST anomalies in the interior Pacific and cool SST anomalies along the North American coast (Mantua et al., 1997).

NAO is defined through surface SLP difference between the Azores high and the Iceland low. Its positive phase is characterized by below-normal pressure and heights over the extra-tropical North Atlantic and above-normal pressure levels over the Central Atlantic and Western Europe. Opposite pattern of heights and pressure levels is manifested during the negative NAO phase. Changes in precipitation patterns and temperature over eastern North America and western Europe are associated with both NAO phases through the modulation of zonal and meridional heat and moisture transport patterns (Hurrell, 1995). The NAO reveals significant inter-seasonal and interannual variability, often with prolonged periods of several months for both positive and negative phases.

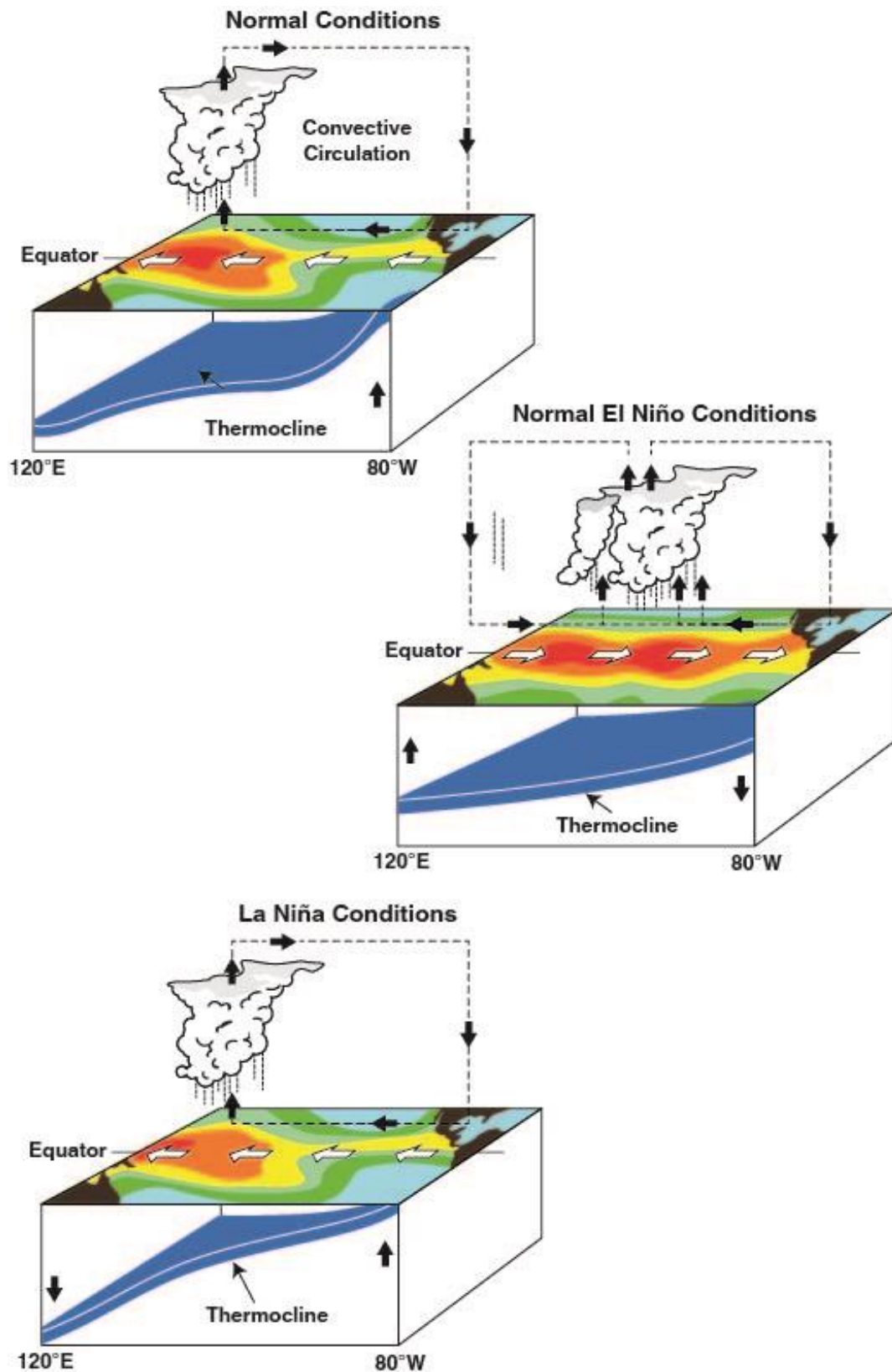


Figure 2. Schematic diagrams showing the weather and ocean conditions associated with normal conditions (top), El Niño (middle), and La Niña (bottom). Figure courtesy of the National Oceanic and Atmospheric Administration (NOAA).

2.2. Well-known dependencies between selected modes of variability

Teleconnections between modes of climate variability (Wallace and Gutzler, 1981) are known to exist. Several authors have conducted studies on the lagged correlations and possible teleconnections between different modes of climate variability (Ambaum et al., 2001; Meehl and Teng, 2007; Meehl and Van Loon, 1979; Wang et al., 2012; Wyatt et al., 2012).

It is believed from Luo et al. (2010) that a better prediction and understanding of El Niño can be provided through studying the effect of IOD on El Niño. Under specific circumstances, the western Pacific surface wind anomalies associated with basin-wide ocean warming or cooling (as a lagged response to El Niño or La Niña) might in turn influence the El Niño decay or onset during certain seasons (Kug et al., 2005; Kug et al., 2006). In fact, this positive feedback, called Bjerknes feedback, can be manifested for example through the equatorial upwelling driven by the cooling induced easterly wind anomalies. The upwelling reinforces in turn the SST cooling (Saji et al., 1999). This ENSO forced basin-wide signal happens essentially through an adjustment of the atmospheric Walker circulation (Klein et al., 1999). Extreme IOD events, generated by air-sea coupling in the tropical IO, can excite large-scale diabatic heating anomalies which consequently alter the Walker circulation and development of ENSO over the equatorial region. A fraction of the basin-wide warming is found to be generated by the reduced wind speeds that diminish the upward latent heat flux and cloud coverage, resulting in more solar radiation reaching the surface (Klein et al., 1999).

Near-surface air temperatures, humidity, winds and cloud distribution change through ENSO-driven circulation patterns. In fact, the atmosphere plays the role of a bridge connecting the equatorial Pacific to the rest of global oceans. This results in variations in surface temperatures, salinity, layer depth and ocean currents that are associated with fluxes of freshwater (Deser et al., 2010). Despite the fact that the air-ocean interactions that are normally responsible for ENSO are fixed over the equatorial regions of the Pacific, changes in the tropical precipitation pattern affect atmospheric circulation on a global level. This is mainly due to the excitation of Rossby waves that spread towards the extra tropics reaching remote areas and consequently affecting other modes of climate variability such as PNA. Having preferred locations, these planetary waves are linked with high-pressure systems over the subtropical regions and low-pressure systems over the midlatitude regions of the North and South Pacific. Overall, the ENSO response is found to be affected by several factors including the wave energy path associated with the structure of wind fields, the different origins and sinks of Rossby waves, as well as the fluctuations in storm tracks (Liu and

Alexander, 2007; Trenberth et al., 1998). Wang and Picaut (2004) summarized the physics behind the mechanisms affecting equatorial Pacific SSTs as follows:

- Atmospheric bridge (through which decadal variability of mid-latitude-generated winds extends to tropics impacting ENSO)
- Subtropical Rossby waves (decadal variability generated by delayed feedback of oceanic Rossby waves that cross the Pacific)
- Advection of temperature anomalies by the subtropical thermohaline cell

A number of studies suggested the connection between dominating modes of variability in the North Pacific (NP) and the North Atlantic (NA), notably between PNA and NAO. Honda et al. (2001) studied this connection using the NCEP reanalysis data between 1973 and 1994 and found a negative correlation (-0.7) between the Aleutian low and the Icelandic Low. Then, Song et al. (2009) investigated the teleconnection on a daily time scale, concluding that the correlation between PNA and NAO happens with mainly no time lag and generally within ± 10 days range for lagged correlations. Other studies, e.g. (Chang, 2004), suggested that correlations between NP and NA change on decadal time scale, with respect to Northern Hemisphere winter storm tracks. Chang (2004) noticed a considerable positive link between regions of winter activity during the 1976 to 1998 period, compared to low correlations during the previous period of 1958 to 1972. These periods actually coincide with the positive and the preceding negative phases of the other main mode of climate variability in the North Pacific; PDO. PDO, the SST anomaly-based mode of variability, combined with ENSO, are positively correlated with the PNA. Thus, a link between NAO and PDO is to be expected. The combined PDO and ENSO effect on PNA is studied by Yu and Zwiers (2007) and was found to vary between periods where PDO/ENSO are in phase and where PDO/ENSO are out of phase. Yu and Zwiers (2007) suggested, through using 1,000-year long integration of the Canadian Centre for Climate Modelling and Analysis (CCCma) coupled climate model, that the in-phase combination of ENSO and PDO ensures the transport of anomalous atmospheric energy from both the Tropical Pacific and the North Pacific towards North America. This favors the occurrence of stationary wave anomalies and therefore leads to PNA-like wave anomaly structures. In contrast, the study shows that anomalies are insignificant when the two modes are out-of-phase. In order to study the modulation of the ENSO effects by the PDO, a similar regime-oriented analysis is to be followed in this thesis to study the varying causal structure between the selected modes of variability during periods with in-phase combination of PDO and ENSO and other periods of out-of-phase combination of the two modes.

3. DATA

3.1. Climate model simulations

In this Master thesis, climate model simulations from models participating in the Coupled Model Intercomparison Project Phase 6 (Eyring et al., 2016a) are analysed. The thesis makes use of different experiments, in particular the pre-industrial control (piControl) simulation, the historical simulation as well as future projections under different scenarios. The piControl simulation is analysed to study dependency structures in the modes of variability in an unforced simulation. A pre-industrial coupled atmosphere/ocean control run relies on unchanged pre-industrial conditions, including prearranged atmospheric concentrations or non-changing gas emissions, aerosols or their precursors. It also simulates an unperturbed land use (Eyring et al., 2016a). The CMIP historical simulations are driven by historical forcings based as much as possible on observations over the 1850-2014 period. They include: emissions of short-lived species and long-lived greenhouse gases (GHGs), solar forcing, stratospheric aerosol data, etc ... Future climate change projections are carried out as part of the Scenario Model Intercomparison Project (ScenarioMIP), which is the primary CMIP6-Endorsed Model Intercomparison Project (MIP) within CMIP6 that provides “multi-model climate projections based on alternative scenarios of future emissions and land use changes produced with integrated assessment models” (O'Neill et al., 2016). ScenarioMIP proposes a set of climate projections based on shared socioeconomic pathways (SSPs) and the Representative Concentration Pathways (RCP). Two of these scenarios are analysed in this thesis: the SSP245, a combination of SSP2 and RCP4.5 which presents a scenario of medium forcing (4.5 W m^{-2}) by the year 2100 and not extreme land use and aerosol pathways. SSP585 scenario, a combination of RCP8.5 and SSP5, is a scenario with high greenhouse gas emissions to produce a high radiative forcing by the year 2100 (8.5 W m^{-2}).

The main analysis in this thesis is based on historical simulations and compares the dependency structures to those from reanalysis datasets (see Section 3.2). The analysis in this thesis is restricted to the CMIP6 models listed in Table 1. Some of the models are also used in the analysis for piControl and ScenarioMIP simulations. The analysis through this thesis is divided into two experimental sets. Each part uses a different combination of the available CMIP6 models.

Table 1. CMIP6 models, their atmosphere and ocean components, and the simulations used in this thesis. All the models listed were used in the analysis on the historical simulation. Highlighted are the models used in the regime-oriented analysis example (see section 5.2)

Model name	Institute	Components		Simulation used		
		Atmosphere	Ocean	piControl	SSP245	SSP585
BCC-CSM2-MR	BCC	BCC-AGCM3-MR	MOM4-L40v2	YES	YES	YES
BCC-ESM1	BCC	BCC-AGCM3-Chem	MOM4-L40v2	NO	NO	NO
CanESM5	CCCma	CanAM5	NEMO & CMOC (for biogeochemistry)	YES	YES	YES
CESM2	NCAR	Community Atmosphere Model (CAM)	Parallel Ocean Program (POP)	NO	NO	NO
MIROC6	MIROC	CCSR-NIES	CCSR Ocean Component model (COCO)	YES	YES	YES
MPI-ESM1-2-HR	MPI	ECHAM6.3	MPIOM1.63	YES	YES	YES
MRI-ESM2-0	MRI	MRI-AGCM3.5	MRI.COMv4	NO	NO	NO
GISS-E2-1-G	NASA-GISS	ModelE	GISS ocean model	NO	NO	NO

3.2. Reanalysis data for model evaluation

Running the PCMCi method on time series from reanalyses and analysing the results compared to the models presents an assessment of how models perform compared to reality. For this purpose, reanalysis datasets are used. These datasets combine measurements with a weather forecast model designed to provide an accurate realistic representation of global atmospheric conditions. Monthly data from the reanalysis dataset by the National Centre for Atmospheric Prediction (NCEP) and the National Centre for Atmospheric Research (NCAR) NCEP–NCAR (Kalnay et al., 1996) is used in this thesis. This global dataset runs from 1948 to now with a 6-hourly, daily or monthly temporal resolution.

4. METHODS

This section presents the basic set of tools and methods through which the study of dependency structures is performed. Sections 4.1 and 4.2 present the tools used for the data extraction and pre-processing: the NCAR CVDP package that is integrated in the ESMValTool. The PCMCI method within the causality detection python package Tigramite is described in Section 4.3.

4.1. NCAR Climate Variability Diagnostics Package (CVDP)

In order to extract the major modes of climate variability in the CMIP model simulations and in reanalyses data, the National Centre for Atmospheric Research (NCAR) Climate Variability Diagnostics Package (CVDP, Phillips et al. (2014)) is used. The CVDP is an analysis tool for the evaluation of the major modes of internal climate variability in climate models. It includes diagnostics to extract the Pacific Decadal Oscillation (PDO), Atlantic Multi-decadal Oscillation (AMO), El Nino-Southern Oscillation (ENSO), North Atlantic Oscillation (NAO), Pacific North and South American (PNA and PSA) patterns and many more (Deser et al., 2004). Its pre-processor includes regridded data for different climatic variables such as: precipitation (pr), skin temperature (ts), air-surface temperature (tas) and sea-level pressure (psl). This diagnostic package prints out time series for the major modes of climate variability that can then be used as input to Tigramite (see Section 4.3). Table 2 provides a description of the calculations of these indices with the CVDP.

Table 2. Description of Indices used during the regime-oriented analysis as calculated by CVDP.

Index	Description	Area	Reference
Niño3.4	ENSO index that accounts for area-averaged SST anomalies (in °C)	5°S-5°N, 120°W-170°W	Trenberth (1997)
IOD	also referred to as Dipole Mode Index (DMI), it denotes the SST anomaly difference between the western equatorial Indian Ocean and south-eastern equatorial Indian Ocean	(10°S-10°N, 50°E-70°E) and (10°S-0°N, 90°E-110°E)	Saji and Yamagata (2003).
PNA	obtained through forming seasonal or annual PSL averages and applying the cosine of latitude weighting. The PNA accounts for the 1 st EOF computed over the respective area.	20°-85°N, 120°E-120°W	Wallace and Gutzler (1981)
PDO	obtained as the leading principal component (PC) of North Pacific area-weighted SST* anomalies (SST* here means that the global mean SST anomaly has been removed at each timestep). Pattern is then created by regressing SST anomalies onto the normalized PC timeseries at each grid box.	20°N-70°N, 110°E-100°W	Deser et al. (2010)
NAO	constructed through seasonal (annual) PSL averages, to which the square root of the cosine of latitude weighting is applied. The leading EOF and associated principal component (PC) timeseries are then calculated over the North Atlantic region. Pattern is finally created by regressing global PSL anomalies (in hPa) onto the normalized PC timeseries.	20°N-80°N, 90°W-40°E	Hurrell and Deser (2009)

As some of the time series of the indices contain a trend, a detrending is necessary before the causality detection algorithm is applied. The trends in the various indices are generally a mixture of forced and internal components. Hence, one should note that when detrending, at least a portion of the internal forcing component is removed.

4.2. ESMValTool

The NCAR CVDP is integrated in the Earth System Model Evaluation Tool (ESMValTool) which is a software package that can be used to evaluate Earth System Models (ESMs). Its diagnostic and performance metrics build the framework for a routine comparison of single models (against the models' pre-existing versions or against observational datasets) or multiple models from MIPs such as CMIP (Meehl et al., 2000). The first aim of the tool has been to tackle a series of systematic biases existing for ESMs (Eyring et al., 2016b). The ESMValTool is designed by a community of developers in such a way that it facilitates the exchange of source code, diagnostic features, and CMIP evaluation results. It is considered as a powerful tool for the improvement of ESMs. The main routines of the ESMValTool are presently written in Python. The diagnostics and plotting functions are based on the NCAR Command Language (NCL), Python or R. Figure 3, shows the structure of the tool, from pre-processing the input data to diagnostics before finally reaching the desired output format (Eyring et al., 2016b). This work is done using the most recent release, ESMValTool v2.0 (Eyring et al., 2019a; Righi et al., 2019).

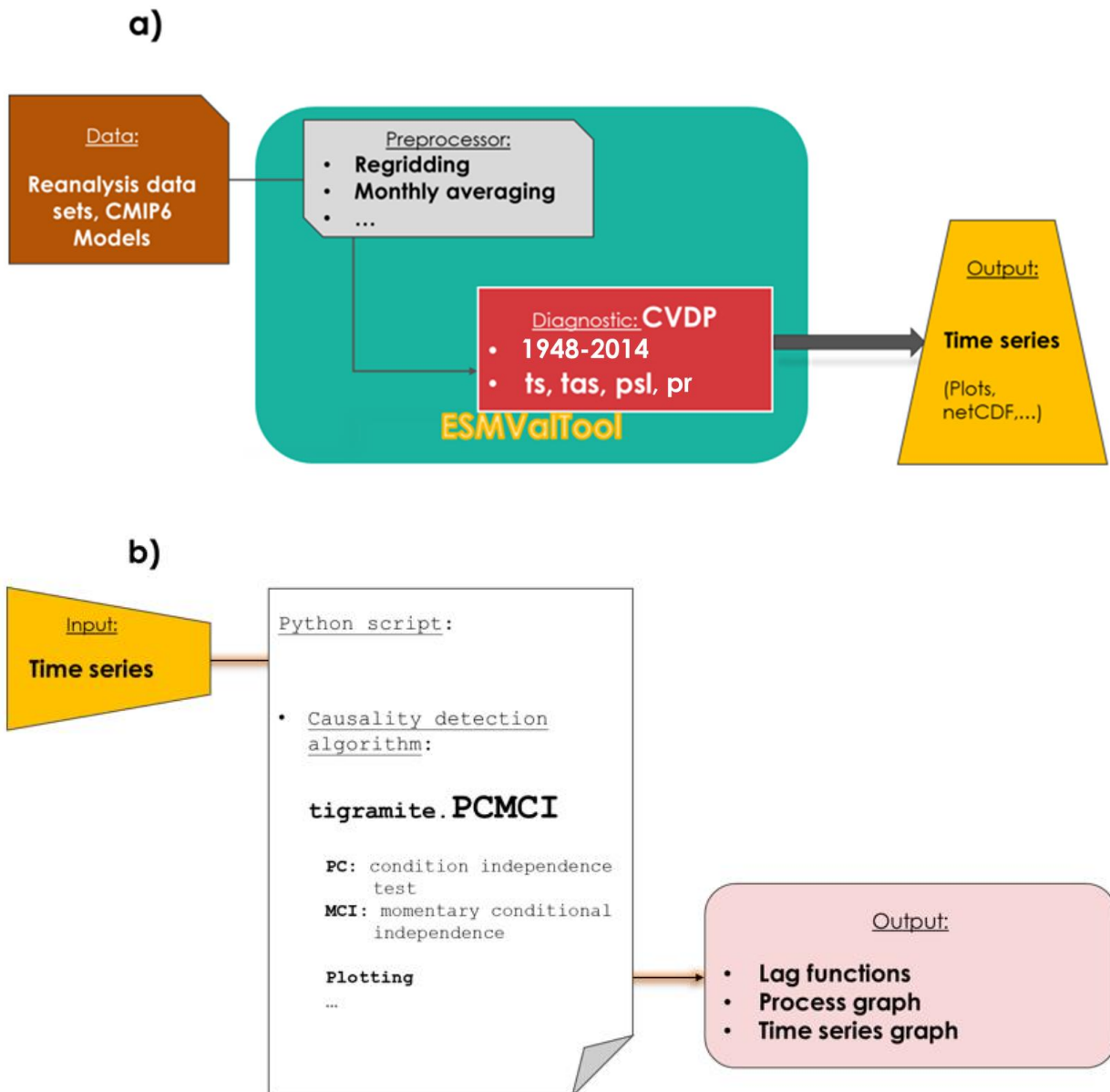


Figure 3. Schematic of the two-step approach during the causality analysis. Part **a**: the process followed to produce the time series for variables and indices using the CVDP implemented inside the ESMValTool. Part **b**: Causality analysis using PCMCI, taking as input the time series produced in part a.

4.3. Tigramite for Causality detection: PCMCI

Tigramite is a python package designed for the causal analysis of time series by Runge et al. (2017). Its main feature is that it allows a graphical causal reconstruction from input time series datasets. These high dimensional time series are analysed with high detection power for dependency structures so that they can be studied for causal analyses. The main method which is used within Tigramite is called PCMCI (Peter Clark Momentary Conditional Independence) which was proven, through analytical experimental results and wide-ranging numerical tests, to outperform

the other approaches when dealing with interdependent time series with high dimensions (Runge et al., 2017).

The approach is built in the context of conditional independence adapted to a high interdependency framework. PCMCI involves two stages: PC and MCI (Runge et al., 2017).

- (1) The first stage is applying the PC_1 (Figure.4 a) Markov set discovery algorithm which is based on the PC algorithm (named after its inventors, Peter Spirtes and Clark Glymour). This algorithm performs a condition selection in order to recognize and detect relevant conditions for every variable contained within the time series (Runge et al., 2017). This stage serves to eliminate irrelevant conditions for all variables by applying independence tests through successive iterations. In its first iteration, after initializing the parent nodes, the algorithm removes the variables that are uncorrelated first. During the second iteration, the algorithm eliminates those variables which showed high association during the first iteration but were revealed, during the second iteration, to be conditionally independent from the driver of the parent node. The algorithm then continues by applying the independence test iteratively, eliminating every variable which happens to be independent conditionally to the two strongest drivers. This is how PC_1 systematically narrows the list of potential conditions to only few relevant ones. However, this adaptive method at this stage also comprises some false positives. The issue is then tackled during the second stage of the method.
- (2) The momentary conditional independence (MCI) test uses the few low dimensional conditions from the earlier stage to establish conditional independence (Figure.4 b). At this stage, indirect and common links are identified. While the earlier conditions are enough to conclude the conditional independence, additional conditions on the parents regarding autocorrelation are the key to the proper false positive control.

A full description of the methods with their respective algorithms is presented in Runge et al. (2017).

To perform the desired regime-oriented analysis, mask type “y” is used. Hence, the independent tests carried out during the different iterations of the PCMCI consider variables only during the non-masked period. However, the parents that drive these variables (other variables or the same one at different past time steps) can come also from the masked period.

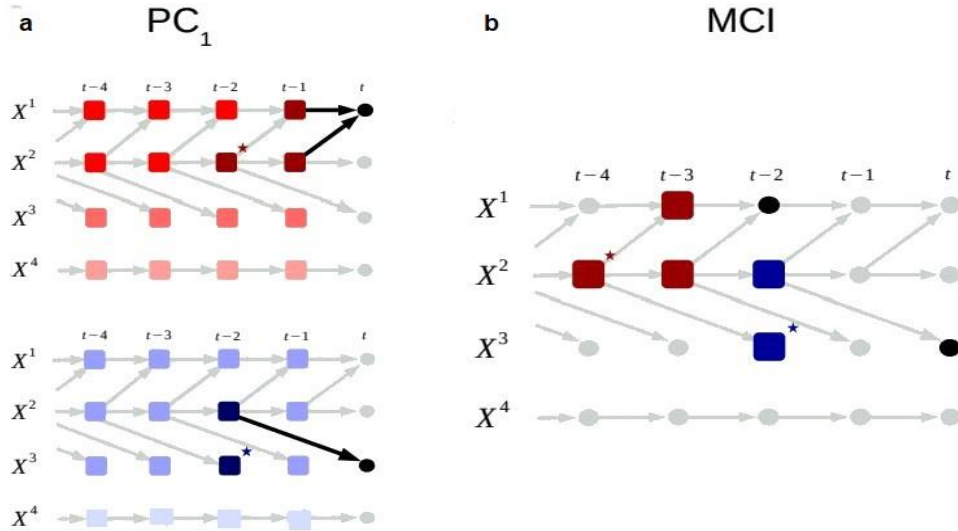


Figure.4 Schematic of the causal discovery method PCMC1. **a)** The PC_1 condition selection algorithm for the variables X^1 (top) and X^3 (bottom): by iteratively removing the conditionally independent variables, the PC_1 algorithm converges to a small set of relevant conditions (dark red/blue) with the potential presence of some false positives (boxes with asterisk). **b)** The obtained low-dimensional conditions are then used during the MCI. The conditions, $\hat{\rho}(X_t^3)$ (parents of X_t^3 , blue boxes) are sufficient to establish conditional independence for testing $X_{t-2}^1 \rightarrow X_t^3$. The remaining conditions $\hat{\rho}(X_{t-2}^1)$ (red boxes) are used to estimate the strength of the causal effect. Figure courtesy of Runge et al. (2017).

5. RESULTS

This section explains, first in section 5.1, the methodology to be followed by reconstructing an example set from the study by Runge et al. (2014) on teleconnections between surface-air temperatures (TAS) over Eastern and Western Europe, in addition to the interplay between sea level pressure anomalies over the Western Pacific and air-sea surface temperature anomalies over both the Central and Eastern Pacific. Section 5.2 presents the regime-oriented causal discovery for the interplay between five major modes of climate variability.

5.1. Reconstruction of climate examples

To test and explain the main procedure adopted for the analysis, CMIP6 models are evaluated with respect to their ability in reproducing two of the results from Runge et al. (2014) where the authors present the two-step procedure to interpret lagged correlations and regressions (in the presence of autocorrelation) for climatic cases. The first example illustrates the teleconnection between surface air temperature (TAS) anomaly indices between one region over western Europe (WEUR) at $45^\circ\text{--}55^\circ\text{N}$, $0^\circ\text{--}10^\circ\text{E}$ and a region over eastern Europe (EEUR) at $45^\circ\text{--}55^\circ$, $40^\circ\text{E}\text{--}50^\circ\text{E}$. WEUR and EEUR are the indices representing the monthly surface temperature anomalies averaged over their corresponding regions. In the other example, the connection between surface temperature and pressure anomalies between three regions are studied. WPAC is the index for the monthly averaged surface sea level pressure (SLP) anomaly over the western Pacific region at $5^\circ\text{S}\text{--}5^\circ\text{N}$,

150E°– 130°E. CPAC and EPAC are the indices for the TAS anomalies over the central Pacific region at 5°S–5°N, 120W°– 150°W and the eastern Pacific region at 5°S–5°N, 80W°– 100°W, respectively. The reference time series for the indices of both examples are taken from the NCEP–NCAR reanalysis dataset (Kalnay et al., 1996) with a time coverage of 780 months from 1948–2012. In addition to the observational reanalysis dataset (NCEP), the PCMCI is performed for five CMIP6 models and their multi-model mean: BCC-ESM1, BCC-CSM2-MR, MRI-ESM2-0, CanESM5, MIROC6. The regional averages are produced using the ESMValTool’s pre-processor. For these examples, the algorithm is set to a maximum time lag $\tau_{\max} = 8$ months and a significance level $\alpha=0.01$.

Figure 5 is produced by the Tigramite python package and shows the process graph representing the lagged dependency for the simple European example, using the observational reanalysis dataset NCEP. The resulting teleconnection between WEUR and EEUR agrees with the lagged cross correlation results from Runge et al. (2014). The 1-month weak lagged correlation also matches the characteristic time scale for turbulent heat transfer between two distant regions represented by two points separated by a distance L : $t_* = L^2/4K$ with $L \approx 3 * 10^6 m$ and $K \approx 10^6 m^2 s^{-1}$. This results in $t_* = 2,25 * 10^6 s = 26 days$ which is approximately 1 month (Runge et al., 2014; Stone and Yao, 1987). The estimation falls in agreement with the atmospheric planetary Rossby waves responsible for the heat exchange between western and eastern Europe on the macro-turbulent synoptic-scale. The waves are found to act on a monthly time scale with a noticeable seasonality characteristic (Palmén and Newton, 1969).

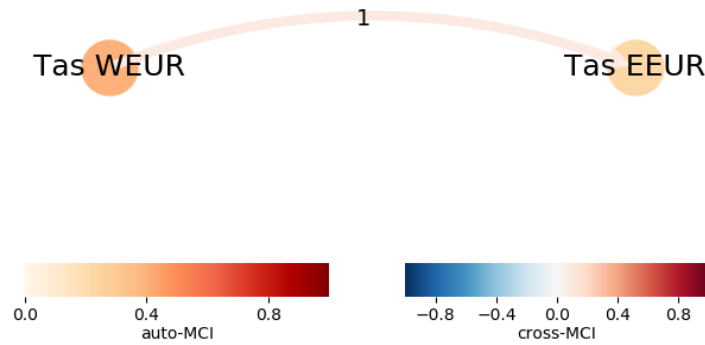


Figure 5. Process graph aggregating information of causal effect of surface air temperature (TAS) anomalies between WEUR and EEUR. Node colour, representing the auto-MCI value, denotes the maximum absolute auto-dependency. The link colour represents cross-MCI value, and link label the time lag (in months). This result is produced using Tigramite for the reference dataset NCEP.

The cross-MCI value exemplifies the lagged cross-dependency between the two constructed indices; i.e. link strength. Whereas the auto-MCI represents the auto-dependency for each variable. The PCMCI is then applied for the selected CMIP6 models in addition to their multi-model mean.

To compare model output with that of the observational NCEP reference dataset, Figure 6 summarizes the links found by applying the PCMCI using the different datasets. This comparison is a way to evaluate the ability of climate models in terms of reproducing teleconnections between different climate indices. The CanESM5 model produces a teleconnection from TAS WEUR to TAS EEUR with 1-month time lag similar to that of the reference dataset. The BCC-CSM2-MR model, on the other hand, produces a link from TAS EEUR to TAS WEUR. The multi-model mean, averaging the results from the five CMIP6 models used, finds in addition the main teleconnection at 1-month time lag, a slightly weaker link with a 5-month time lag in the same direction. Moreover, the multi-model mean also generates opposite direction (TAS EEUR \rightarrow TAS WEUR) positive links with 7 and 3-month time lags.

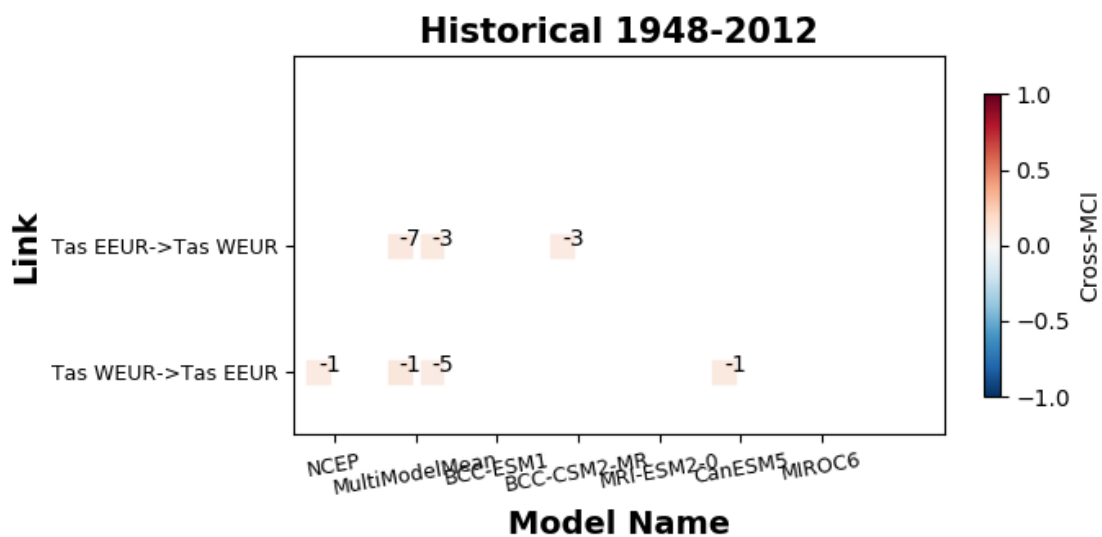


Figure 6. Summary of link strengths (cross-MCI values) according the dataset used. The colour of the boxes denotes the cross-MCI value of the link. The labels on the boxes refer to the time lag for which the teleconnection is found to be effective. MIROC6 and MRI-ESM2-0 do not produce any links at $\alpha=0.01$.

In the next example, also from Runge et al. (2014), the dependency structure between WPAC, CPAC and EPAC is studied using the PCMCI through Tigramite. Figure 7 shows the process graph representing the EPAC \rightarrow CPAC \rightarrow WPAC \rightarrow EPAC loop using the NCEP dataset and the Multi-model mean (average of the 5 CMIP6 models). The basic mechanism behind these teleconnections is the tropical convective transport driven by the Walker circulation (Hosking et al., 2012). The associated Walker circulation is mostly determined by heating on the western verges of the equatorial oceans. During normal and La Niña phases, ENSO is mainly driven by the strong

supply of moisture in the lower troposphere over the western Pacific. This introduction of significant moisture is associated with the ENSO-induced pronounced sensible and latent heats (Runge et al., 2014). The EPAC→CPAC→WPAC circulation favours upwelling over the eastern Pacific Ocean and downwelling over western Pacific. As oceanic temperatures decrease with depth, an increase in SLP over the western Pacific (WPAC) accompanied with a decrease in TAS would result in an increase in sea and air temperature TAS over the central and eastern regions of the Pacific (CPAC and EPAC). Figure 8 shows a detailed summary of the links between the three variables. All models reproduce the contemporaneous cross correlation between EPAC and CPAC (found by the reference dataset NCEP with a cross-MCI of 0.34), with varying cross-MCI values (link strengths) between 0.23 and 0.38. All models also reproduce the 1 month lagged EPAC → CPAC link with a significantly higher positive cross-MCI compared to the NCEP reanalysis data. Interestingly, all models produce positively lagged cross-correlations CPAC → WPAC which is not produced by NCEP at $\alpha=0.01$ but found by Runge et al. (2014) where $\alpha=0.05$ was used. The CanESM5, MIROC6 and MRI-ESM2-0 models agree with the reference dataset in constructing similar-strength WPAC → EPAC links, with varying time lags $0 < \tau \leq 3$ months. Negatively lagged WPAC → CPAC connections are produced by all models.

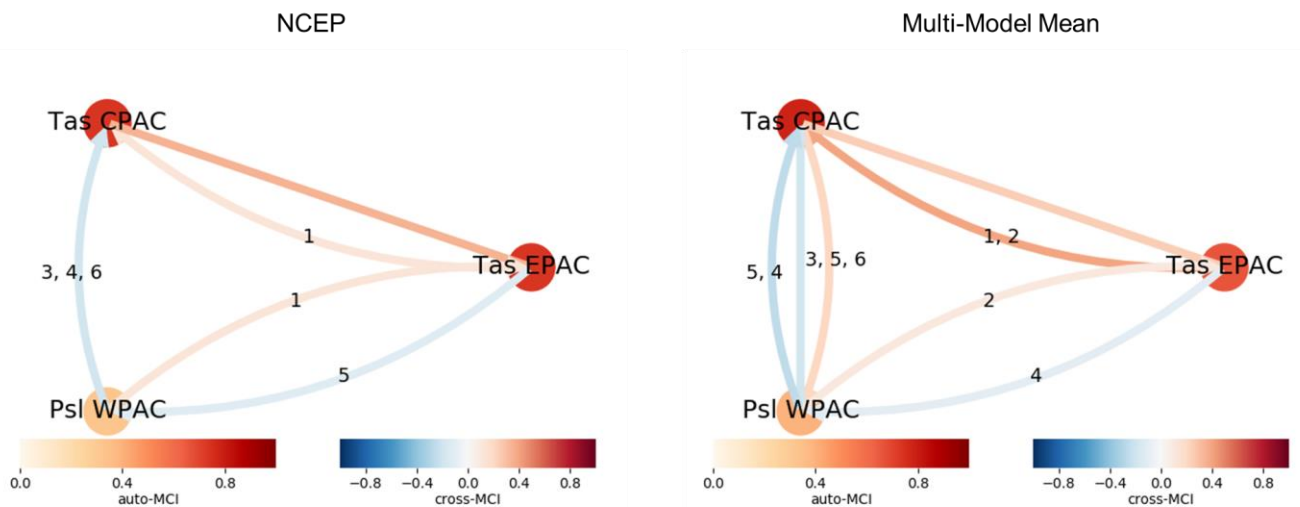


Figure 7. Process graph aggregating information of causal effect of surface air temperature (TAS) and surface pressure (PSL) anomalies over EPAC, CPAC and WPAC. Node colour denotes auto-MCI value, link colour cross-MCI value, and link label the time lag (in months). When a link has more than one time-lag label, the link colour denotes the link with the highest absolute cross-MCI value; time lags are sorted according to their $|\text{cross-MCI}|$. Undirected non-curved links denote contemporaneous connections happening at a time lag $\tau < 1$ month. This result is produced using Tigramite for the reference dataset NCEP (left) and the Multi-model mean of the 5 CMIP6 models (right).

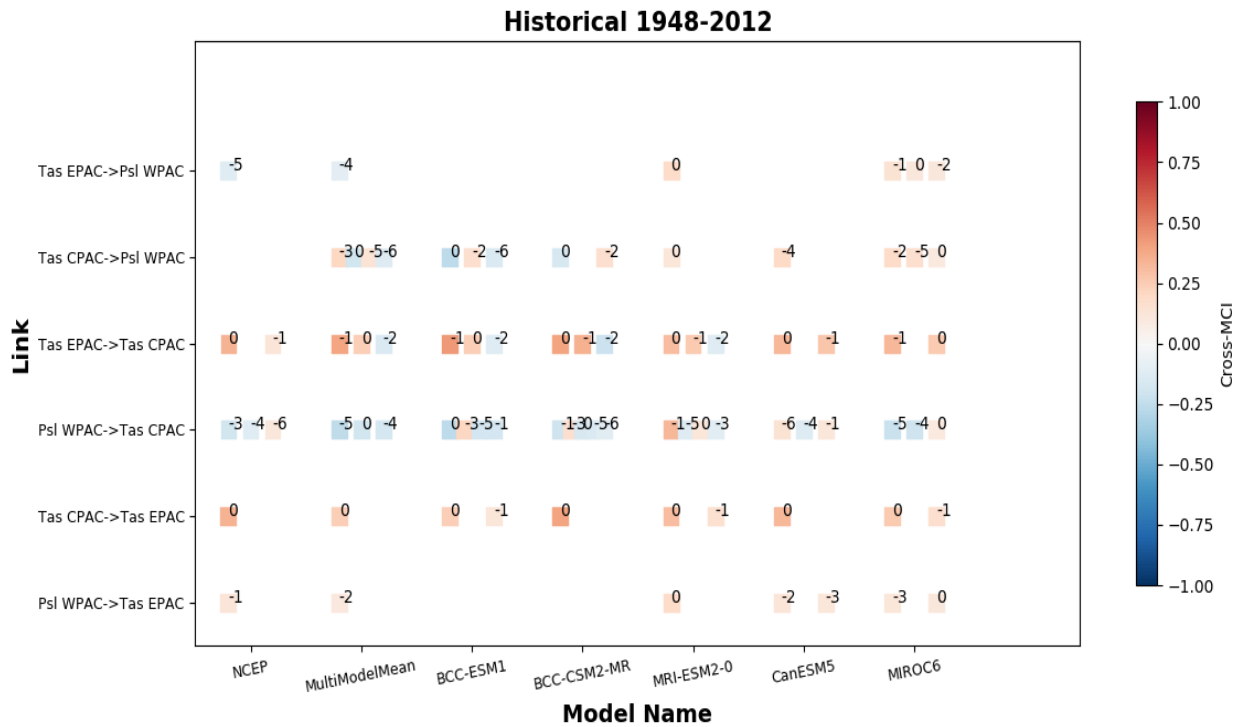


Figure 8. Summary of the links produced according the dataset used. A 0-month time lag denotes a contemporaneous undirected link between the variables happening at a time lag shorter than 1 month. These links are shown twice in the figure. NCEP is the only dataset to not produce a positive lagged CPAC→WPAC connection (at alpha=0.01).

5.2. Regime-oriented causal discovery

Dependency structures between teleconnections could change depending on the actual state of the climate. Hence, understanding the mechanisms that drive the causal dependencies in the Earth System during specific events or well-defined periods is of high significance. Therefore, in this section PCMCI is used to study regime-oriented dependency structures of modes of climate variability. The time series are again extracted using the CVDP implemented within the ESMValTool for the indices from monthly mean data, here: Nino34, IOD, PDO, NAO and PNA indices (see definition in Table 2).

Like in the previous section, a causality analysis is conducted using the PCMCI method, this time with the five detrended time series of climate variability indices as variables. The NCEP dataset is used as reference for the period between start 1948 and end of 2014 (804 months). The following six CMIP6 climate models are used in the same analysis of historical data and their results are compared to the reference reanalysis dataset: MIROC6, MPI-ESM1-2-HR, BCC-CSM2-MR, CanESM5, CESM2 and GISS-E2-1-G. The free parameter of the algorithm, the maximum time lag, τ_{\max} is considered to be 9 months. This choice of τ_{\max} is done after investigating the lagged dependencies plot (for the NCEP reanalysis), showing the matrix of time lagged (auto)correlations

(see Figure 9). It could be assumed that all dependencies decay after a maximum period of 9 months. The significance level was set to $\alpha=0.01$ in this example.

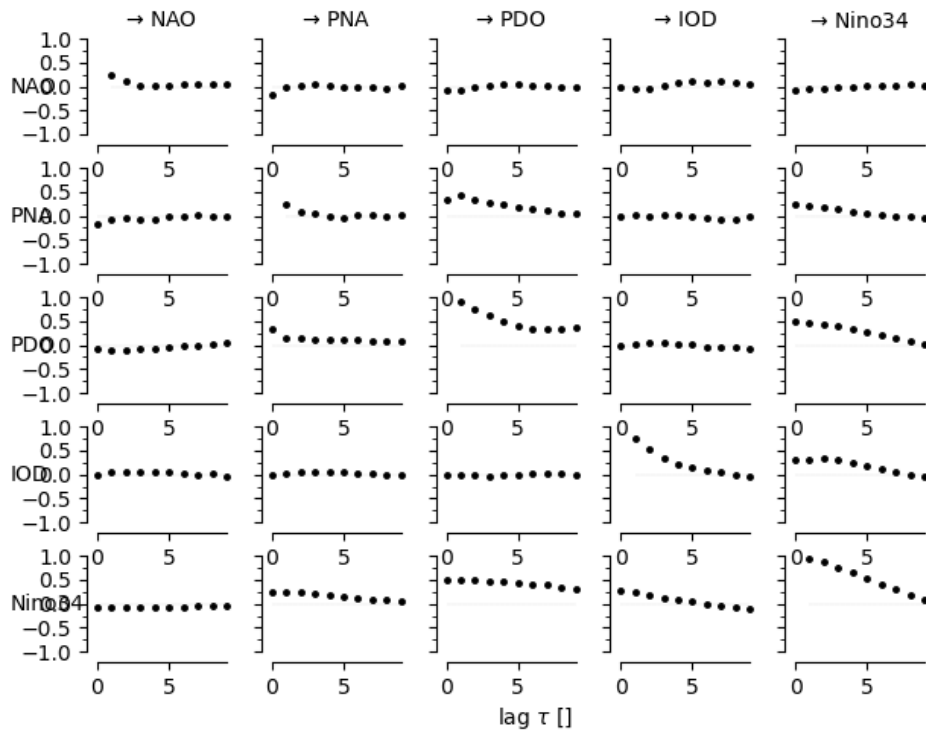


Figure 9. Matrix of lag functions between the five indices: NAO, PNA, PDO, IOD and Nino34 (conditional on the past of all-time series up to $\tau_{\max} = 9$ months). This result is produced using Tigramite

The regime-oriented approach aims to construct a dependency structure linking the five modes of climate variability during specific regimes or periods. For this purpose, the masking feature within Tigramite is used in order to mask first, all time steps where PDO and ENSO out of phase, and then apply opposite masking for the reversed phase analysis. Figure 10 shows the time series for the indices during time period of PDO and ENSO in phase (black) and out of phase (grey) using the NCEP dataset. Results of both masking conditions are compared to analyse how the regime change affects the dependency structures between the different modes.

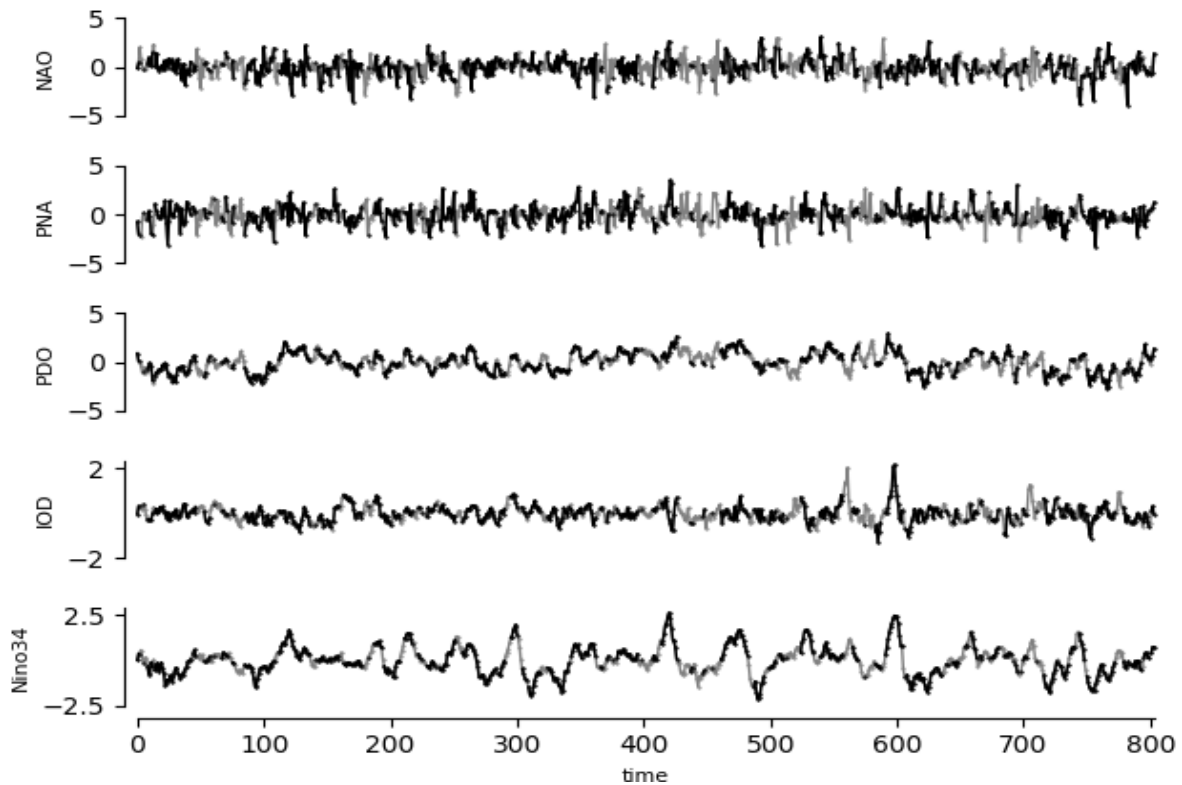


Figure 10. Time series for NAO, PNA, PDO, IOD and Nino34 indices, computed by CVDP using the NCEP reanalysis dataset for the 1948-2014 period (804 months). Grey shaded area is the masked period of the time series when PDO and ENSO are out of phase. Figure produced by Tigramite.

Figure 11 shows the process graph summarizing the most significant causal pathways between the different modes for three cases: when no mask is applied (the complete time series is taken into account), when PDO and ENSO are in phase (during PDO+/El Niño and PDO-/La Niña), and when PDO and ENSO are out of phase (during PDO+/La Niña and PDO-/El Niño). The change in the causal structure between the two regimes agrees with literature by Yu and Zwiers (2007) and Wang et al. (2014) who suggest that the ENSO induced effects (e.g. in the North Pacific and/or Indian Ocean) cancel out when PDO and ENSO are not in the same phase. Nino34—IOD, and Nino34—PDO links are therefore only present for the PDO/ENSO in-phase combination (see Figure 11).

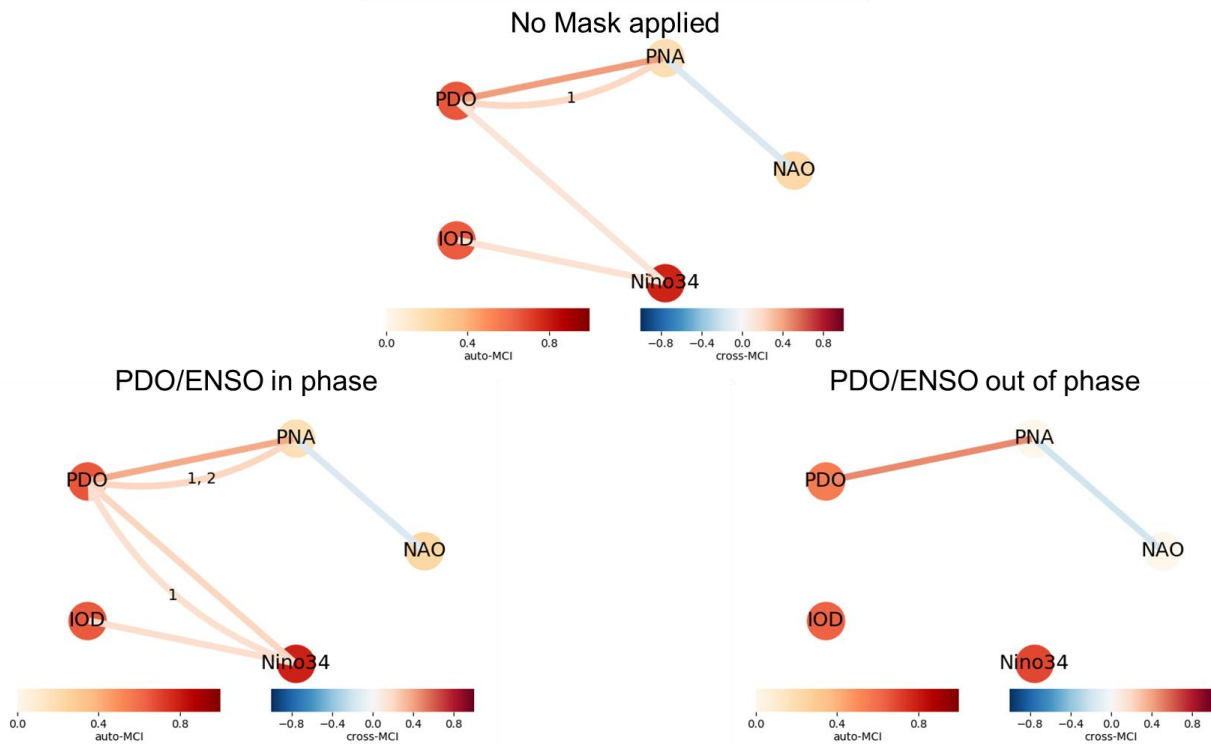


Figure 11. Process graphs aggregating the causal effect between the five indices (modes) for the unmasked whole time series (top), the in-phase combination of PDO and Nino34 (bottom left) and the out-of-phase combination of PDO and Nino34 (bottom right). Graphs are produced by Tigramite for the 1948-2014 period using the NCEP reanalysis dataset.

This “regime-oriented” analysis, as the name suggests, helps understanding the mechanisms that drive the causal dependencies in the Earth System during “specific periods/events”. Some causal links are magnified, weakened, or even (dis)appear when switching from a regime to another. These changes can therefore not be tracked if the independence tests carried during the PCMCI are not restricted to any time period (see top of Figure 11).

As shown in Figure 12, for the unmasked whole time series of the historical simulations (1948-2014), all 6 CMIP6 models reproduce the strong PNA–PDO link and the negatively cross-correlated NAO–PNA link (except MIROC6 for the latter). However, Nino34–IOD connections are only reproduced by MIROC6 and CESM2 models. The positive Nino34–PDO connection is reproduced by 4 of the 6 models. A slightly negative PDO–NAO connection (not found using NCEP) is produced by all models (except MIROC6). The interplay between the two modes is yet suggested by studies where NCEP-NCAR data were used to study storm track correlations between the NP and NA (Chang, 2004) and the relationship between NAO and early warm season temperatures in the Southwestern United States in an interplay with PDO, AMO and ENSO (Myoung et al., 2015). Figure 13 presents a summary plot for the auto-MCI values for the same run (no regime selection). Auto-MCI values of the variables are mostly consistent for all datasets.

The process graph, through the node colour, accounts only for maximum absolute auto-MCI values. Negative auto-MCI values can be well spotted through the time series graph produced by Tigramite (see Appendix 2.), while the process graph plots like in Figure 11 only show the maximum auto-MCI value. Although the process graph efficiently represents the causal effects between the variables, the time series graph is a better output for understanding the spatio-temporal framework of the dependency structure through the displayed causal pathways.

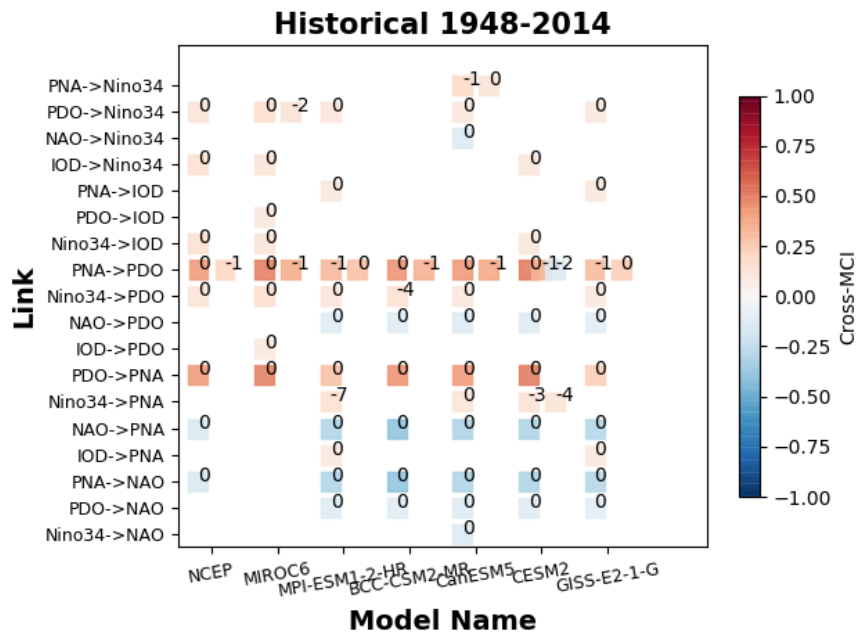


Figure 12. Summary plot for the links produced during a non-filtered (no mask applied) PCMCI run of historical data (1948-2014) using NCEP and different CMIP6 models, numbers denote the time lag. Notice that contemporaneous undirected links (lag=0) are displayed twice.

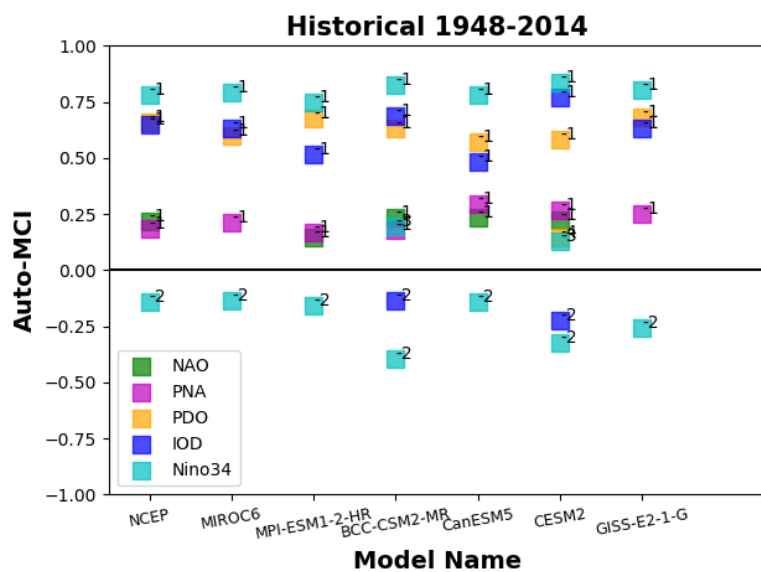


Figure 13. Summary of Auto-MCI values for the same run (as Figure 12) depending on the dataset used. Box color denotes the variable, box label denotes the lag of the auto-correlation.

It is worthwhile to look at how the models perform during the regime-oriented analysis. For this purpose, a result comparison can be made from Figure 14. The difference in the number of links found is clear. The results from when PDO/ENSO are in the same phase are similar to those from the entire period regarding the well-established connections: PNA—PDO, NAO—PNA, PDO—NAO, Nino34—IOD. The similarity is mainly because PDO, with its ENSO-like pattern, is most of the time in the same phase as ENSO (Figure 10; black lines) compared to when they are in opposite phases (Figure 10; grey lines). In contrast, the out-of-phase combination shows how Nino34 connections decay during this regime. Only CanESM5 model finds an insignificant negative Nino34—NAO cross-correlation. This is expected as literature (Wang et al. (2014); Yu and Zwiers (2007)) suggest that the basin-wide ENSO teleconnections weaken as the modulation effect by the PDO cancels out when the two modes are in opposite phases (i.e. during PDO+/La Nina and/or PDO-/El Nino). As the small portion of ENSO induced PNA variability cancels out during the out-of-phase regime, the PNA—PDO connection becomes significantly important. NCEP and most of the models produce higher PNA—PDO cross-MCI values when PDO and ENSO are not in the same phase. The negative NAO—PNA connection is also found to be slightly stronger during the out-of-phase regime.

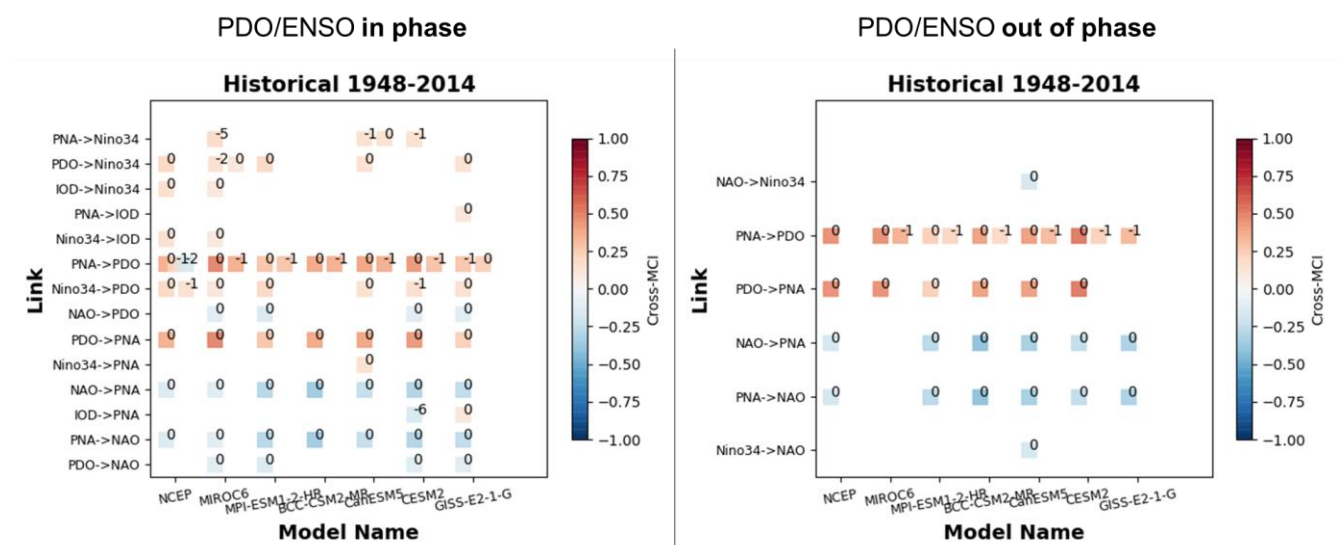


Figure 14. The same as Figure 12 but for different regimes. To the left are the links found during the PDO/ENSO in-phase regime. The plot on the right contains links produced for the PDO/ENSO out-of-phase regime.

An important question is how the regime-oriented dependency structures change if an unforced simulation is analysed and how they change in the future. Therefore, in addition to the historical simulations, the piControl and future scenario simulations are analysed. The performed piControl simulation is an unforced simulation using unchanged pre-industrial conditions of 1850 for 153 years (imitation of 1948-2100 period with pre-industrial conditions). Comparing this to historical

simulations can be used to determine the forced response. The future scenarios, SSP245 and SSP585, are simulations according to different emission pathways and are used for the 2014-2100 period. A summary of the links for the PDO/ENSO in-phase regime found in 4 CMIP6 models for the piControl simulations is shown in Figure 15, and for the SSP245 and SSP585 future scenario simulations in Figure 16. MIROC6, MPI-ESM1-2-HR, BCC-CSM2-MR and CanESM5 are the 4 CMIP6 models used in these simulations. The respective results for the out-of-phase regime are shown in Appendix Figure 5.

The strong connections are well found for the 4 models (with MIROC6 missing again the NAO—PNA negative cross-correlation). The other strong PDO—PNA connection is interestingly not produced by BCC-CSM2-MR nor CanESM5 for the SSP585 scenario (found for all other simulations). MIROC6 is found to produce slight negative IOD connections only during the SSP245 simulation. Noteworthy, is the fact that MPI-ESM1-2-HR and BCC-CSM2-MR find no Nino34—PDO connection for the SSP245 scenario, while this connection is found by these models for all other simulations.

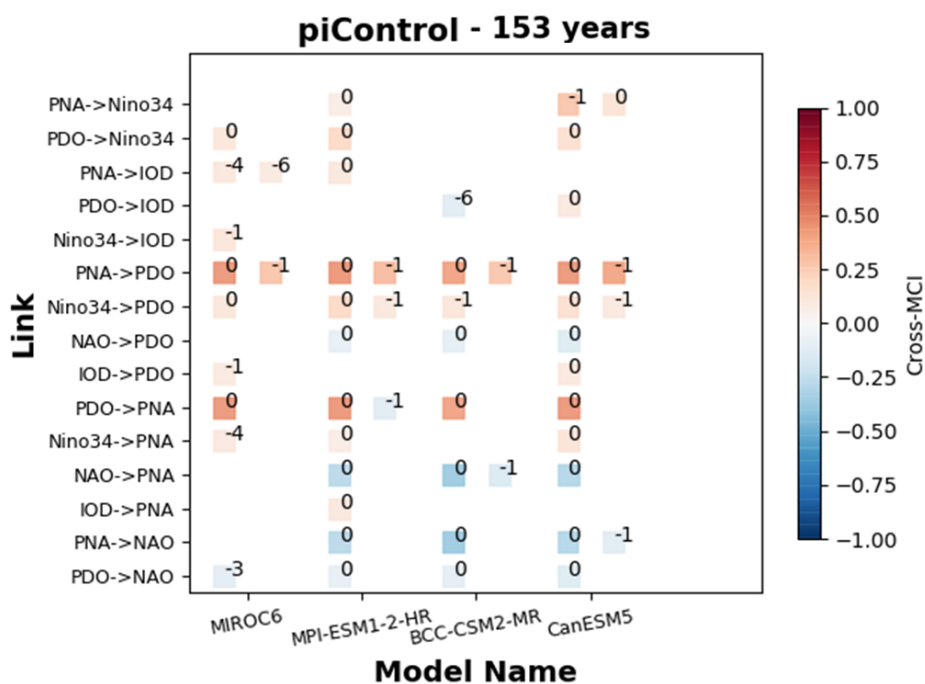


Figure 15. Summary plot for the links produced during a PCMC1 run for a piControl run simulating the 1948-2100 (153 years) period for the PDO/ENSO in-phase regime, numbers denote the time lag. Notice that contemporaneous undirected links (lag=0) are displayed twice. Results for 4 CMIP6 models.

PDO/ENSO in phase

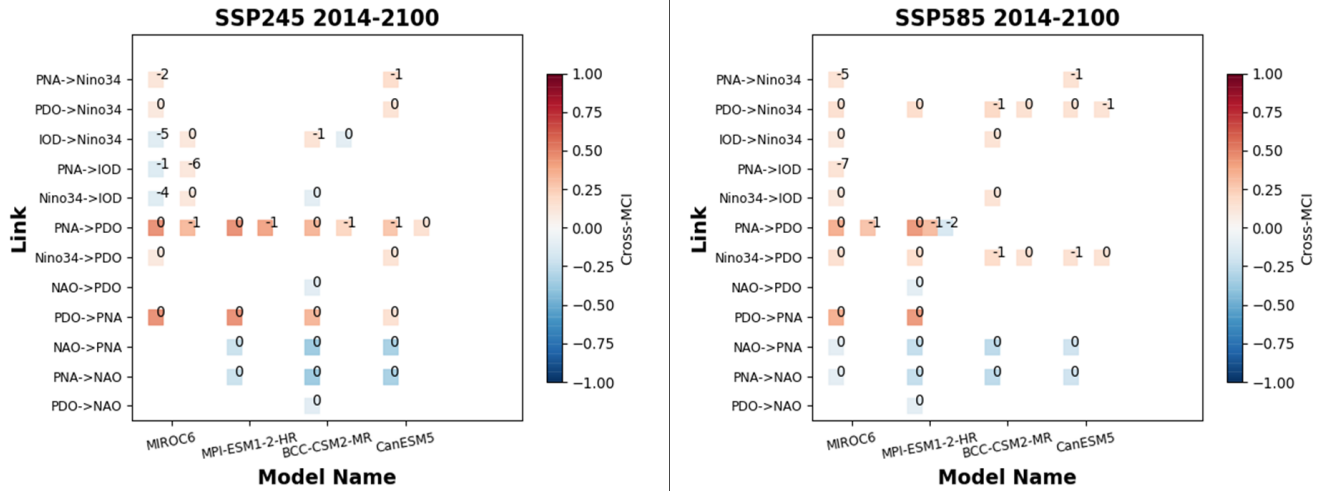


Figure 16. The same as Figure 15 but for SSP245 (left) and SSP585 (right) simulating the 2014-2100 (87 years) period.

In order to separate the forced response from the natural variability, a comparison between the historical and piControl simulations is valuable. This allows to track how the dependency structures for CMIP6 models change between historical simulations (based as far as possible on observations) and piControl simulations (based on pre-industrial conditions). Ideally, this method helps drawing conclusions on how the forced component of climate variability affects the causal network between the different modes. Figure 17 is a comparison of the summary of links found during a historical simulation (left) and piControl simulation (right) using unmasked data. It is found that more connections are detected during the piControl simulation. While the strong well-established connections are consistent through both simulations, the models produce additional low |cross-MCI| links when simulating pre-industrial conditions.

No Mask applied

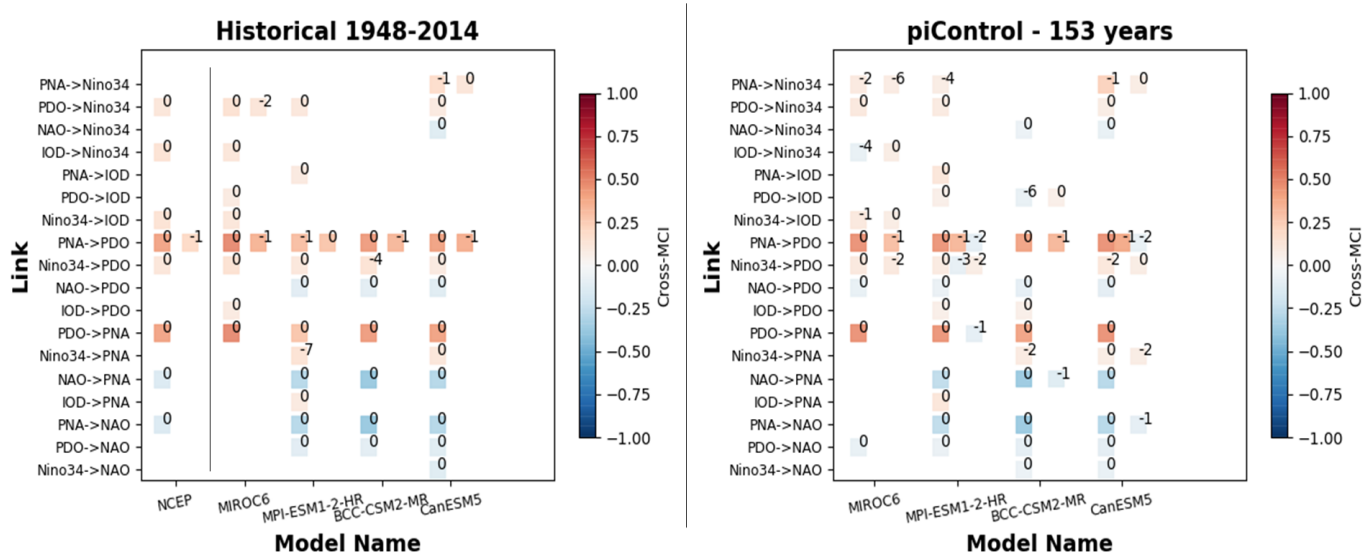


Figure 17. Summary plots for the links produced during a PCMRI run for historical simulation (left) and 153-year piControl simulation (right). Both results were produced using unmasked data.

The reason why the piControl produces much more links than the future scenario simulations (Figure 15 vs Figure 16) may be due to the length of the time series. It produces more links than all other simulations including the historical simulations (Figure 17). In fact, longer time series are important to reveal hidden weak teleconnections that might not be found when using short-length time series. A similar piControl simulation as in Figure 17 but for a shorter 67-year time series (imitating the time length of historical and reanalysis data 1948-2014) was found to produce a significantly lower number of connections compared to the 153-year simulation. A summary plot for this 67-year piControl simulation compared to the 153-year simulation is presented in Appendix Figure 6.

It was already suggested that ENSO teleconnections, for instance, will change due to the warmer climate (Meehl and Teng, 2007) and/or due to the increased anthropogenic forcing that affects the atmospheric circulation (Yeh et al., 2018). Still, it is difficult based on only the results presented in this thesis, to associate the changes in Nino34 connections to anthropogenic forcing.

6. DISCUSSION

Reconstruction of benchmark examples from Runge et al. (2014) provided an assessment of 5 CMIP6 models in terms of the ability of the models to reproduce the EPAC \rightarrow CPAC \rightarrow WPAC \rightarrow EPAC feedback loop. BCC models (BCC-ESM1 and BCC-CSM2-MR) are found to not produce any WPAC–EPAC link. On average, based on the multi-model mean, the 5 models reproduce the feedback loop. However, they also produce additional links that are not detected in the reanalysis data. Reanalysis data incorporate observations dataset and are used as a reference for comparison because they provide the most accurate picture of the real world. The PNA–PDO is an example of well-established connections; both originating from the North Pacific, the modes co-vary with strong correlation. The PDO’s local and remote effects are closely associated to atmospheric Aleutian low (AL) variability (Zhang et al., 2018). AL is a part of the quadrupole pattern for the SLP anomaly differences that define PNA; hence, the strong connection to PDO. The positive correlation could also be explained in the presence of ENSO. The warm phase of ENSO (El Niño) is known to excite the PNA, extending across the North Pacific and reaching North America with AL as a centre of action (Horel and Wallace, 1981). A positive PDO phase is then driven by the strengthened AL through surface heat fluxes and wind-driven mixing (Alexander et al., 2002).

A key scientific issue to discuss is the ability of climate models to simulate causal pathways between different modes of climate variability. This has been proven to be true (at least for historical simulations) for most of the well-established connections including: the highly positively correlated PNA–PDO connection, the negative NAO–PNA and PDO–NAO connections, and the Nino34–IOD teleconnection. The models were able to reproduce the links with relatively similar link strengths (cross-MCI values) and time lags as the reference dataset (NCEP). On the other hand, some connections are found only when using model data, and still physical explanation can be found in various literature. However, it is unclear if the found connections are actually produced because the models generate the right mechanisms for these teleconnections to happen. For instance, the Nino34 \rightarrow PNA link is only produced by three models with different time lags ($0 \leq \tau \leq 7$ months). A similar connection is in fact, proposed by several authors (Yu and Zwiers (2007); Kwon et al. (2013); Yeh et al. (2018)), but conclusion cannot be made on whether the connection is simulated for the right reasons or not. Different ensemble members could be analysed (possibly in future work) in order to investigate the potential changes in the causal structures. This would provide an additional evaluation criterion to find out whether the teleconnection mechanisms of the models persist from an ensemble member to another.

It should be mentioned that time series have been de-trended for all variables after their computation by CVDP and before using them as input for the PCMCI. The trends in the various indices are generally a mixture of forced and internal variability. Thus, de-trending is expected to remove at least part of the internal variability component. To overcome this issue in the future, de-trending is to be performed with respect to piControl simulations; this allows to separate the forced response from the natural variability.

The role of the filter is of considerable significance for the regime-oriented analysis presented in this paper. The filter, or the masking condition, permits the analysis of causal structures during specific events/periods. Similar analysis can be carried out for different masking conditions (e.g. Winter vs Summer months); these kinds of phase-targeted studies allow a better understanding of the hidden mechanisms or teleconnections that may not appear when studying year-long time series. As it can be seen from Figures 12 and 14, the results from the unfiltered data englobe roughly the sum of links present in both regimes. Yet, the same data analysed for different lengths of time series produce different causal networks (not shown). The use of datasets spanning a longer time range is crucial to overcome this issue. This is to say that the length of the timeseries is important for the PCMCI; the longer the time series, the less chance of missing out possible significant links.

Therefore, a longer time series was used for piControl (153 years) and the future scenarios (87 years). In addition to the longer time series, the unforced simulation of pre-industrial emission levels provides more periodic time series with less abrupt fluctuations. It is assumed that these two factors explain the large set of links found using the piControl simulation. The future scenario results (SSP245 and SSP585) from the PDO/ENSO out-of-phase regime look different to those from the in-phase regime, with only the connection between the major North Pacific modes (PDO—PNA) being present for both phases and through most of the datasets. A noteworthy exception to this conclusion is implied in the fact that two models do not always produce the connection when simulated through SSP585. This marks the change induced by a different emission/radiative forcing simulation (SSP585 vs SSP245), where some models predict a weakening of PDO—PNA connections under strong radiative forcing. In general, the future scenarios are able to recapture the strong causal links found during the historical simulation but it is difficult to draw conclusions from the present results on how different emission pathways change the dependency networks. In addition to the CMIP6 simulations used in this thesis, an analysis of the 4xCO₂ simulations compared to pre-Industrial era might be helpful. Moreover, different new SSP scenarios are introduced for the latest CMIP phase. They simulate different combinations of shared socio-economic pathways (SSPs) and Representative Concentration Pathways (RCPs, (O'Neill et al.,

2016)). It is yet to prove how this regime-oriented analysis for future scenarios can improve (multi)decadal forecasts when associated with modes of (multi)decadal variability (e.g. PDO, Atlantic Multi-decadal Oscillation (AMO), etc...).

7. CONCLUSIONS

The dynamical processes for the ocean-atmosphere interactions change from one model to another, resulting in different teleconnection patterns. Therefore, the model comparison with respect to a well-established reference observational dataset is, nowadays, a noteworthy assessment method of the extent to which climate models truly simulate the wide-ocean basin and atmospheric long lagged teleconnections within the global Earth System. This thesis summarized the results where CMIP6 models were evaluated for their ability to reproduce dependency structures between 5 major modes of climate variability: NAO, PNA, PDO, ENSO and IOD. 5 out of 6 models were able to simulate the decay of ENSO dependencies when the mode is in the opposite phase as PDO. The strong connections PNA–PDO and NAO-PNA were not only found to persist through all historical model simulations, but were also produced in a pre-industrial control and future scenario simulations. This is true with the exception that the connection between PDO and PNA is weakened or not found for the SSP585 scenario for two models. The presented approach is believed to provide new incentives in terms of improving decadal predictions. High-dimensional causal networks are constructed for a better visualization of the causal process linking a variable to another. This visualization (through causal graphs) allows easy interpretation of causal strength and time lags after which the connection is found to be effective. The introduced regime-oriented analysis revealed hidden changes in the dependency structure between the modes of climate variability, changes that cannot be noticed when analysing the whole time series. When applied to future simulations, the regime-oriented analysis using PCMCI can determine how the causal networks may change in the future, providing room for the improvement of interannual and/or decadal predictions and the possible assessment of socio-economic impacts on various remote areas. Examining changes in dependency structures in the major modes of variability in future scenarios and further separating the forced response from internal climate variability is of high relevance for climate projections. The analysis of these changes can help to understand the anthropogenic impact on the widely spread teleconnections in our Earth System.

Acknowledgement. *We acknowledge the World Climate Research Programme, which, through its Working Group on Coupled Modelling, coordinated and promoted CMIP6. We thank the climate modelling groups for producing and making available their model output, the Earth System Grid Federation (ESGF) for archiving the data and providing access, and the multiple funding agencies who support CMIP6 and ESGF.*

8. REFERENCES

- ALEXANDER, M.A., BLADÉ, I., NEWMAN, M., LANZANTE, J.R., LAU, N.-C. AND SCOTT, J.D., 2002. THE ATMOSPHERIC BRIDGE: THE INFLUENCE OF ENSO TELECONNECTIONS ON AIR–SEA INTERACTION OVER THE GLOBAL OCEANS. *JOURNAL OF CLIMATE*, 15(16): 2205-2231.
- AMBAUM, M.H., HOSKINS, B.J. AND STEPHENSON, D.B., 2001. ARCTIC OSCILLATION OR NORTH ATLANTIC OSCILLATION? *JOURNAL OF CLIMATE*, 14(16): 3495-3507.
- ANDERSON, D.L. AND WILLEBRAND, J., 2013. *DECADAL CLIMATE VARIABILITY: DYNAMICS AND PREDICTABILITY*, 44. SPRINGER SCIENCE & BUSINESS MEDIA.
- BJERKNES, J., 1969. ATMOSPHERIC TELECONNECTIONS FROM THE EQUATORIAL PACIFIC1. *MONTHLY WEATHER REVIEW*, 97(3): 163-172.
- CHANG, E.K., 2004. ARE THE NORTHERN HEMISPHERE WINTER STORM TRACKS SIGNIFICANTLY CORRELATED? *JOURNAL OF CLIMATE*, 17(21): 4230-4244.
- DE VIRON, O., DICKEY, J.O. AND GHIL, M., 2013. GLOBAL MODES OF CLIMATE VARIABILITY. *GEOPHYSICAL RESEARCH LETTERS*, 40(9): 1832-1837.
- DESER, C., ALEXANDER, M.A. AND TIMLIN, M.S., 2003. UNDERSTANDING THE PERSISTENCE OF SEA SURFACE TEMPERATURE ANOMALIES IN MIDLATITUDES. *JOURNAL OF CLIMATE*, 16(1): 57-72.
- DESER, C., ALEXANDER, M.A., XIE, S.-P. AND PHILLIPS, A.S., 2010. SEA SURFACE TEMPERATURE VARIABILITY: PATTERNS AND MECHANISMS. *ANNUAL REVIEW OF MARINE SCIENCE*, 2: 115-143.
- DESER, C., PHILLIPS, A.S. AND HURRELL, J.W., 2004. PACIFIC INTERDECADAL CLIMATE VARIABILITY: LINKAGES BETWEEN THE TROPICS AND THE NORTH PACIFIC DURING BOREAL WINTER SINCE 1900. *JOURNAL OF CLIMATE*, 17(16): 3109-3124.
- EBBESMEYER, C.C., CAYAN, D.R., MCLAIN, D.R., NICHOLS, F.H., PETERSON, D.H. AND REDMOND, K.T., 1991. 1976 STEP IN THE PACIFIC CLIMATE: FORTY ENVIRONMENTAL CHANGES BETWEEN 1968-1975 AND 1977-1984.
- EYRING, V., BOCK, L., LAUER, A., RIGHI, M., SCHLUND, M., ANDELA, B., ARNONE, E., BELLPRAT, O., BRÖTZ, B., CARON, L.P., CARVALHAIS, N., CIONNI, I., CORTESI, N., CREZEE, B., DAVIN, E., DAVINI, P., DEBEIRE, K., DE MORA, L., DESER, C., DOCQUIER, D., EARNSHAW, P., EHBRECHT, C., GIER, B.K., GONZALEZ-REVIRIEGO, N., GOODMAN, P., HAGEMANN, S., HARDIMAN, S., HASSLER, B., HUNTER, A., KADOW, C., KINDERMANN, S., KOIRALA, S., KOLDUNOV, N.V., LEJEUNE, Q., LEMBO, V., LOVATO, T., LUCARINI, V., MASSONNET, F., MÜLLER, B., PANDDE, A., PÉREZ-ZANÓN, N., PHILLIPS, A., PREDOI, V.,

- RUSSELL, J., SELLAR, A., SERVA, F., STACKE, T., SWAMINATHAN, R., TORRALBA, V., VEGAS-REGIDOR, J., VON HARDENBERG, J., WEIGEL, K. AND ZIMMERMANN, K., 2019A. ESMVALTOOL v2.0 - EXTENDED SET OF LARGE-SCALE DIAGNOSTICS FOR QUASI-OPERATIONAL AND COMPREHENSIVE EVALUATION OF EARTH SYSTEM MODELS IN CMIP. GEOSCI. MODEL DEV. DISCUSS., 2019: 1-81.
- EYRING, V., BONY, S., MEEHL, G.A., SENIOR, C.A., STEVENS, B., STOUFFER, R.J. AND TAYLOR, K.E., 2016A. OVERVIEW OF THE COUPLED MODEL INTERCOMPARISON PROJECT PHASE 6 (CMIP6) EXPERIMENTAL DESIGN AND ORGANIZATION. GEOSCIENTIFIC MODEL DEVELOPMENT (ONLINE), 9(LLNL-JRNL-736881).
- EYRING, V., COX, P.M., FLATO, G.M., GLECKLER, P.J., ABRAMOWITZ, G., CALDWELL, P., COLLINS, W.D., GIER, B.K., HALL, A.D. AND HOFFMAN, F.M., 2019B. TAKING CLIMATE MODEL EVALUATION TO THE NEXT LEVEL. NATURE CLIMATE CHANGE, 9(2): 102-110.
- EYRING, V., RIGHI, M., LAUER, A., EVALDSSON, M., WENZEL, S., JONES, C., ANAV, A., ANDREWS, O., CIONNI, I. AND DAVIN, E.L., 2016B. ESMVALTOOL (v1.0)—A COMMUNITY DIAGNOSTIC AND PERFORMANCE METRICS TOOL FOR ROUTINE EVALUATION OF EARTH SYSTEM MODELS IN CMIP. GEOSCIENTIFIC MODEL DEVELOPMENT, 9: 1747-1802.
- FLATO, G., MAROTZKE, J., ABIODUN, B., BRACONNOT, P., CHOU, S.C., COLLINS, W., COX, P., DRIOUECH, F., EMORI, S. AND EYRING, V., 2014. EVALUATION OF CLIMATE MODELS, CLIMATE CHANGE 2013: THE PHYSICAL SCIENCE BASIS. CONTRIBUTION OF WORKING GROUP I TO THE FIFTH ASSESSMENT REPORT OF THE INTERGOVERNMENTAL PANEL ON CLIMATE CHANGE. CAMBRIDGE UNIVERSITY PRESS, PP. 741-866.
- FOUNTALIS, I., BRACCO, A. AND DOVROLIS, C., 2015. ENSO IN CMIP5 SIMULATIONS: NETWORK CONNECTIVITY FROM THE RECENT PAST TO THE TWENTY-THIRD CENTURY. CLIMATE DYNAMICS, 45(1-2): 511-538.
- FRANKIGNOUL, C. AND HASSELMANN, K., 1977. STOCHASTIC CLIMATE MODELS, PART II APPLICATION TO SEA-SURFACE TEMPERATURE ANOMALIES AND THERMOCLINE VARIABILITY. TELLUS, 29(4): 289-305.
- GLANTZ, M.H., KATZ, R.W. AND NICHOLLS, N., 1991. TELECONNECTIONS LINKING WORLDWIDE CLIMATE ANOMALIES, 535. CAMBRIDGE UNIVERSITY PRESS CAMBRIDGE.
- GRAHAM, F.S., BROWN, J.N., WITTENBERG, A.T. AND HOLBROOK, N.J., 2015. REASSESSING CONCEPTUAL MODELS OF ENSO. JOURNAL OF CLIMATE, 28(23): 9121-9142.
- GRAHAM, N.E., BARNETT, T.P., WILDE, R., PONATER, M. AND SCHUBERT, S., 1994. ON THE ROLES OF TROPICAL AND MIDLATITUDE SSTs IN FORCING INTERANNUAL TO INTERDECADAL VARIABILITY IN THE WINTER NORTHERN HEMISPHERE CIRCULATION. JOURNAL OF CLIMATE, 7(9): 1416-1441.

- HASSELMANN, K., 1976. STOCHASTIC CLIMATE MODELS PART I. THEORY. *TELLUS*, 28(6): 473-485.
- HONDA, M., NAKAMURA, H., UKITA, J., KOUSAKA, I. AND TAKEUCHI, K., 2001. INTERANNUAL SEESAW BETWEEN THE ALEUTIAN AND ICELANDIC LOWS. PART I: SEASONAL DEPENDENCE AND LIFE CYCLE. *JOURNAL OF CLIMATE*, 14(6): 1029-1042.
- HOREL, J.D. AND WALLACE, J.M., 1981. PLANETARY-SCALE ATMOSPHERIC PHENOMENA ASSOCIATED WITH THE SOUTHERN OSCILLATION. *MONTHLY WEATHER REVIEW*, 109(4): 813-829.
- HOSKING, J.S., RUSSO, M.R., BRAESICKE, P. AND PYLE, J.A., 2012. TROPICAL CONVECTIVE TRANSPORT AND THE WALKER CIRCULATION. *ATMOS. CHEM. PHYS.*, 12(20): 9791-9797.
- HURRELL, J.W., 1995. DECADEAL TRENDS IN THE NORTH ATLANTIC OSCILLATION. *SCIENCE (NEW YORK, N.Y.)*, 269: 676-9.
- HURRELL, J.W. AND DESER, C., 2009. NORTH ATLANTIC CLIMATE VARIABILITY: THE ROLE OF THE NORTH ATLANTIC OSCILLATION. *JOURNAL OF MARINE SYSTEMS*, 78(1): 28-41.
- IPCC, 2013. SUMMARY FOR POLICYMAKERS. IN: C. INTERGOVERNMENTAL PANEL ON CLIMATE (EDITOR), *CLIMATE CHANGE 2013 – THE PHYSICAL SCIENCE BASIS: WORKING GROUP I CONTRIBUTION TO THE FIFTH ASSESSMENT REPORT OF THE INTERGOVERNMENTAL PANEL ON CLIMATE CHANGE*. CAMBRIDGE UNIVERSITY PRESS, CAMBRIDGE, PP. 1-30.
- KALNAY, E., KANAMITSU, M., KISTLER, R., COLLINS, W., DEAVEN, D., GANDIN, L., IREDELL, M., SAHA, S., WHITE, G., WOOLLEN, J., ZHU, Y., CHELLIAH, M., EBISUZAKI, W., HIGGINS, W., JANOWIAK, J., MO, K.C., ROPELEWSKI, C., WANG, J., LEETMAA, A., REYNOLDS, R., JENNE, R. AND JOSEPH, D., 1996. THE NCEP/NCAR 40-YEAR REANALYSIS PROJECT. *BULLETIN OF THE AMERICAN METEOROLOGICAL SOCIETY*, 77(3): 437-472.
- KLEIN, S.A., SODEN, B.J. AND LAU, N.-C., 1999. REMOTE SEA SURFACE TEMPERATURE VARIATIONS DURING ENSO: EVIDENCE FOR A TROPICAL ATMOSPHERIC BRIDGE. *JOURNAL OF CLIMATE*, 12(4): 917-932.
- KUG, J.S., AN, S.I., JIN, F.F. AND KANG, I.S., 2005. PRECONDITIONS FOR EL NINO AND LA NINA ONSETS AND THEIR RELATION TO THE INDIAN OCEAN. *GEOPHYSICAL RESEARCH LETTERS*, 32(5).
- KUG, J.S., LI, T., AN, S.I., KANG, I.S., LUO, J.J., MASSON, S. AND YAMAGATA, T., 2006. ROLE OF THE ENSO–INDIAN OCEAN COUPLING ON ENSO VARIABILITY IN A COUPLED GCM. *GEOPHYSICAL RESEARCH LETTERS*, 33(9).
- KWON, M., YEH, S.-W., PARK, Y.-G. AND LEE, Y.-K., 2013. CHANGES IN THE LINEAR RELATIONSHIP OF ENSO–PDO UNDER THE GLOBAL WARMING. *INTERNATIONAL JOURNAL OF CLIMATOLOGY*, 33(5): 1121-1128.

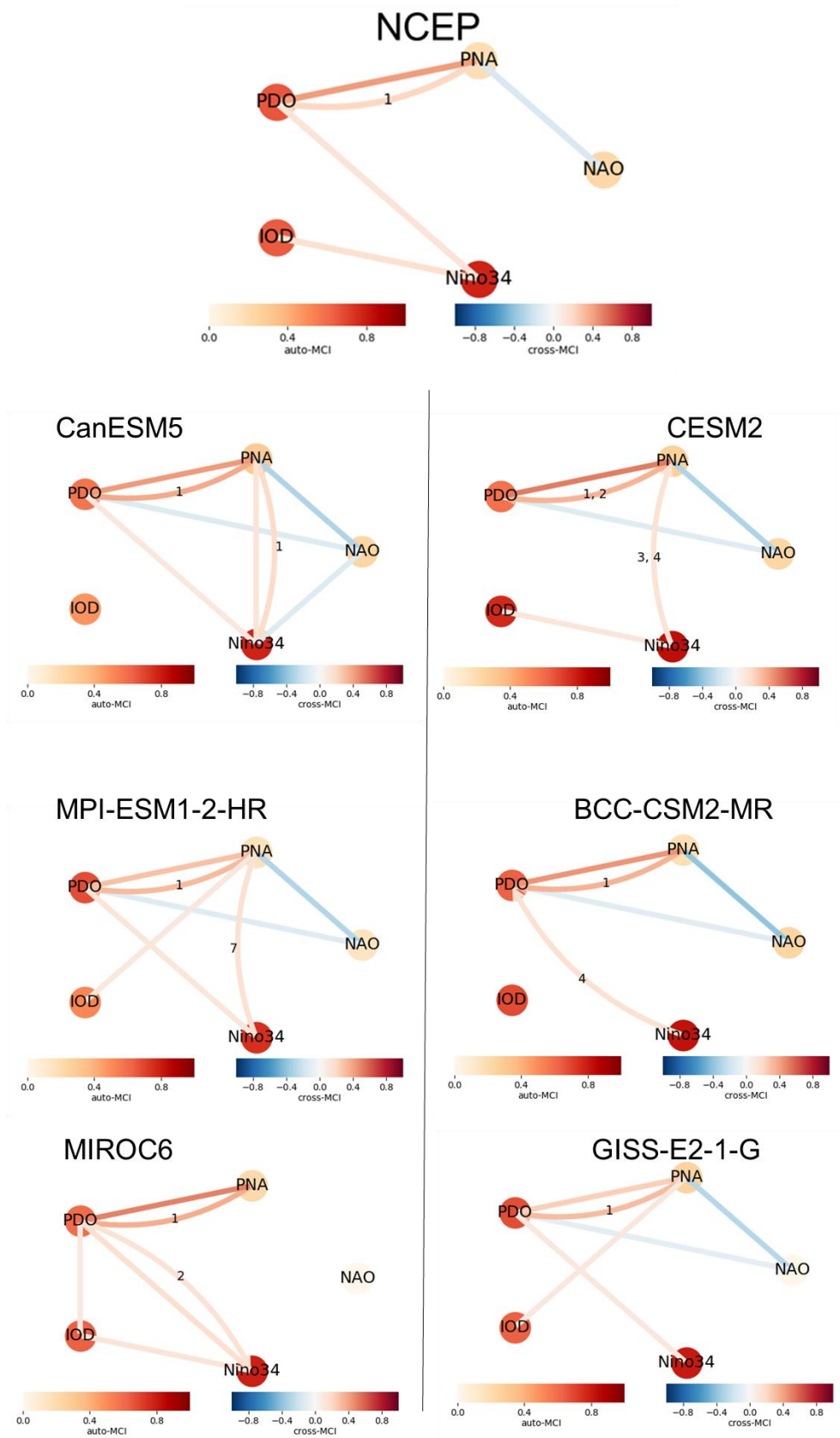
- LAU, N.-C. AND NATH, M.J., 1994. A MODELING STUDY OF THE RELATIVE ROLES OF TROPICAL AND EXTRATROPICAL SST ANOMALIES IN THE VARIABILITY OF THE GLOBAL ATMOSPHERE-OCEAN SYSTEM. *JOURNAL OF CLIMATE*, 7(8): 1184-1207.
- LEATHERS, D.J., YARNAL, B. AND PALECKI, M.A., 1991. THE PACIFIC/NORTH AMERICAN TELECONNECTION PATTERN AND UNITED STATES CLIMATE. PART I: REGIONAL TEMPERATURE AND PRECIPITATION ASSOCIATIONS. *JOURNAL OF CLIMATE*, 4(5): 517-528.
- LIU, Z. AND ALEXANDER, M., 2007. ATMOSPHERIC BRIDGE, OCEANIC TUNNEL, AND GLOBAL CLIMATIC TELECONNECTIONS. *REVIEWS OF GEOPHYSICS*, 45(2).
- LUO, J.-J., ZHANG, R., BEHERA, S.K., MASUMOTO, Y., JIN, F.-F., LUKAS, R. AND YAMAGATA, T., 2010. INTERACTION BETWEEN EL NIÑO AND EXTREME INDIAN OCEAN DIPOLE. *JOURNAL OF CLIMATE*, 23(3): 726-742.
- MANTUA, N.J., HARE, S.R., ZHANG, Y., WALLACE, J.M. AND FRANCIS, R.C., 1997. A PACIFIC INTERDECADAL CLIMATE OSCILLATION WITH IMPACTS ON SALMON PRODUCTION*. *BULLETIN OF THE AMERICAN METEOROLOGICAL SOCIETY*, 78(6): 1069-1080.
- MEEHL, G.A., BOER, G.J., COVEY, C., LATIF, M. AND STOUFFER, R.J., 2000. THE COUPLED MODEL INTERCOMPARISON PROJECT (CMIP). *BULLETIN OF THE AMERICAN METEOROLOGICAL SOCIETY*, 81(2): 313-318.
- MEEHL, G.A. AND TENG, H., 2007. MULTI-MODEL CHANGES IN EL NIÑO TELECONNECTIONS OVER NORTH AMERICA IN A FUTURE WARMER CLIMATE. *CLIMATE DYNAMICS*, 29(7-8): 779-790.
- MEEHL, G.A. AND VAN LOON, H., 1979. THE SEESAW IN WINTER TEMPERATURES BETWEEN GREENLAND AND NORTHERN EUROPE. PART III: TELECONNECTIONS WITH LOWER LATITUDES. *MONTHLY WEATHER REVIEW*, 107(9): 1095-1106.
- MYOUNG, B., KIM, S.H., KIM, J. AND KAFATOS, M.C., 2015. ON THE RELATIONSHIP BETWEEN THE NORTH ATLANTIC OSCILLATION AND EARLY WARM SEASON TEMPERATURES IN THE SOUTHWESTERN UNITED STATES. *JOURNAL OF CLIMATE*, 28(14): 5683-5698.
- O'NEILL, B.C., TEBALDI, C., VAN VUUREN, D.P., EYRING, V., FRIEDLINGSTEIN, P., HURTT, G., KNUTTI, R., KRIEGLER, E., LAMARQUE, J.F., LOWE, J., MEEHL, G.A., MOSS, R., RIAHI, K. AND SANDERSON, B.M., 2016. THE SCENARIO MODEL INTERCOMPARISON PROJECT (SCENARIO MIP) FOR CMIP6. *GEOSCI. MODEL DEV.*, 9(9): 3461-3482.
- PALMÉN, E. AND NEWTON, C.W., 1969. ATMOSPHERIC CIRCULATION SYSTEMS : THEIR STRUCTURE AND PHYSICAL INTERPRETATION.
- PHILLIPS, A.S., DESER, C. AND FASULLO, J., 2014. EVALUATING MODES OF VARIABILITY IN CLIMATE MODELS. *EOS, TRANSACTIONS AMERICAN GEOPHYSICAL UNION*, 95(49): 453-455.

- RANDALL, D.A., WOOD, R.A., BONY, S., COLMAN, R., FICHEFET, T., FYFE, J., KATTSOV, V., PITMAN, A., SHUKLA, J. AND SRINIVASAN, J., 2007. CLIMATE MODELS AND THEIR EVALUATION, CLIMATE CHANGE 2007: THE PHYSICAL SCIENCE BASIS. CONTRIBUTION OF WORKING GROUP I TO THE FOURTH ASSESSMENT REPORT OF THE IPCC (FAR). CAMBRIDGE UNIVERSITY PRESS, PP. 589-662.
- RIGHI, M., ANDELA, B., EYRING, V., LAUER, A., PREDOI, V., SCHLUND, M., VEGAS-REGIDOR, J., BOCK, L., BRÖTZ, B., DE MORA, L., DIBLEN, F., DREYER, L., DROST, N., EARNSHAW, P., HASSLER, B., KOLDUNOV, N., LITTLE, B., LOOSVELDT TOMAS, S. AND ZIMMERMANN, K., 2019. ESMVALTOOL V2.0 – TECHNICAL OVERVIEW. GEOSCI. MODEL DEV. DISCUSS., 2019: 1-28.
- RUNGE, J., BATHIANY, S., BOLLT, E., CAMPS-VALLS, G., COUMOU, D., DEYLE, E., GLYMOUR, C., KRETSCHMER, M., MAHECHA, M.D. AND MUÑOZ-MARÍ, J., 2019. INFERRING CAUSATION FROM TIME SERIES IN EARTH SYSTEM SCIENCES. NATURE COMMUNICATIONS, 10(1): 2553.
- RUNGE, J., NOWACK, P., KRETSCHMER, M., FLAXMAN, S. AND SEJDINOVIC, D., 2017. DETECTING CAUSAL ASSOCIATIONS IN LARGE NONLINEAR TIME SERIES DATASETS. ARXIV PREPRINT ARXIV:1702.07007.
- RUNGE, J., PETOUKHOV, V., DONGES, J.F., HLINKA, J., JAJCAY, N., VEJMEJKA, M., HARTMAN, D., MARWAN, N., PALUŠ, M. AND KURTHS, J., 2015. IDENTIFYING CAUSAL GATEWAYS AND MEDIATORS IN COMPLEX SPATIO-TEMPORAL SYSTEMS. NATURE COMMUNICATIONS, 6: 8502.
- RUNGE, J., PETOUKHOV, V. AND KURTHS, J., 2014. QUANTIFYING THE STRENGTH AND DELAY OF CLIMATIC INTERACTIONS: THE AMBIGUITIES OF CROSS CORRELATION AND A NOVEL MEASURE BASED ON GRAPHICAL MODELS. JOURNAL OF CLIMATE, 27(2): 720-739.
- SAJI, N.H., GOSWAMI, B.N., VINAYACHANDRAN, P.N. AND YAMAGATA, T., 1999. A DIPOLE MODE IN THE TROPICAL INDIAN OCEAN. NATURE, 401(6751): 360-363.
- SAJI, N.H. AND YAMAGATA, T., 2003. POSSIBLE IMPACTS OF INDIAN OCEAN DIPOLE MODE EVENTS ON GLOBAL CLIMATE. CLIMATE RESEARCH, 25(2): 151-169.
- SELVARAJU, R., 2007. CLIMATE VARIABILITY AND CHANGE : ADAPTATION TO DROUGHT IN BANGLADESH : A RESOURCE BOOK AND TRAINING GUIDE / PREPARED BY SELVARAJU RAMAMASY AND STEPHAN BAAS. INSTITUTIONS FOR RURAL DEVELOPMENT ; 9. ASIAN DISASTER PREPAREDNESS CENTER, FOOD AND AGRICULTURE ORGANIZATION OF THE UNITED NATIONS, ROME.
- SONG, J., LI, C., ZHOU, W. AND PAN, J., 2009. THE LINKAGE BETWEEN THE PACIFIC-NORTH AMERICAN TELECONNECTION PATTERN AND THE NORTH ATLANTIC OSCILLATION. ADVANCES IN ATMOSPHERIC SCIENCES, 26(2): 229-239.

- STEINHAEUSER, K. AND TSONIS, A.A., 2014. A CLIMATE MODEL INTERCOMPARISON AT THE DYNAMICS LEVEL. *CLIMATE DYNAMICS*, 42(5): 1665-1670.
- STONE, P.H. AND YAO, M.-S., 1987. DEVELOPMENT OF A TWO-DIMENSIONAL ZONALLY AVERAGED STATISTICAL-DYNAMICAL MODEL. PART II: THE ROLE OF EDDY MOMENTUM FLUXES IN THE GENERAL CIRCULATION AND THEIR PARAMETERIZATION. *JOURNAL OF THE ATMOSPHERIC SCIENCES*, 44(24): 3769-3786.
- STOUFFER, R.J., EYRING, V., MEEHL, G.A., BONY, S., SENIOR, C., STEVENS, B. AND TAYLOR, K.E., 2017. CMIP5 SCIENTIFIC GAPS AND RECOMMENDATIONS FOR CMIP6. *BULLETIN OF THE AMERICAN METEOROLOGICAL SOCIETY*, 98(1): 95-105.
- TIMMERMANN, A., OBERHUBER, J., BACHER, A., ESCH, M., LATIF, M. AND ROECKNER, E., 1999. INCREASED EL NIÑO FREQUENCY IN A CLIMATE MODEL FORCED BY FUTURE GREENHOUSE WARMING. *NATURE*, 398(6729): 694-697.
- TRENBERTH, K.E., 1997. THE DEFINITION OF EL NIÑO. *BULLETIN OF THE AMERICAN METEOROLOGICAL SOCIETY*, 78(12): 2771-2778.
- TRENBERTH, K.E., BRANSTATOR, G.W., KAROLY, D., KUMAR, A., LAU, N.-C. AND ROPELEWSKI, C., 1998. PROGRESS DURING TOGA IN UNDERSTANDING AND MODELING GLOBAL TELECONNECTIONS ASSOCIATED WITH TROPICAL SEA SURFACE TEMPERATURES. *JOURNAL OF GEOPHYSICAL RESEARCH: OCEANS*, 103(C7): 14291-14324.
- WALLACE, J.M. AND GUTZLER, D.S., 1981. TELECONNECTIONS IN THE GEOPOTENTIAL HEIGHT FIELD DURING THE NORTHERN HEMISPHERE WINTER. *MONTHLY WEATHER REVIEW*, 109(4): 784-812.
- WANG, C. AND PICAUT, J., 2004. UNDERSTANDING ENSO PHYSICS—A REVIEW. *EARTH'S CLIMATE: THE OCEAN-ATMOSPHERE INTERACTION*, GEOPHYS. MONOGR, 147: 21-48.
- WANG, G., YANG, P., ZHOU, X., SWANSON, K.L. AND TSONIS, A.A., 2012. DIRECTIONAL INFLUENCES ON GLOBAL TEMPERATURE PREDICTION. *GEOPHYSICAL RESEARCH LETTERS*, 39(13).
- WANG, S., HUANG, J., HE, Y. AND GUAN, Y., 2014. COMBINED EFFECTS OF THE PACIFIC DECADAL OSCILLATION AND EL NIÑO-SOUTHERN OSCILLATION ON GLOBAL LAND DRY-WET CHANGES. *SCI REP*, 4(1): 6651.
- WYATT, M.G., KRAVTSOV, S. AND TSONIS, A.A., 2012. ATLANTIC MULTIDECADAL OSCILLATION AND NORTHERN HEMISPHERE'S CLIMATE VARIABILITY. *CLIMATE DYNAMICS*, 38(5-6): 929-949.
- YEH, S.-W., CAI, W., MIN, S.-K., MCPHADEN, M.J., DOMMENGET, D., DEWITTE, B., COLLINS, M., ASHOK, K., AN, S.-I., YIM, B.-Y. AND KUG, J.-S., 2018. ENSO ATMOSPHERIC TELECONNECTIONS AND THEIR RESPONSE TO GREENHOUSE GAS FORCING. *REVIEWS OF GEOPHYSICS*, 56(1): 185-206.

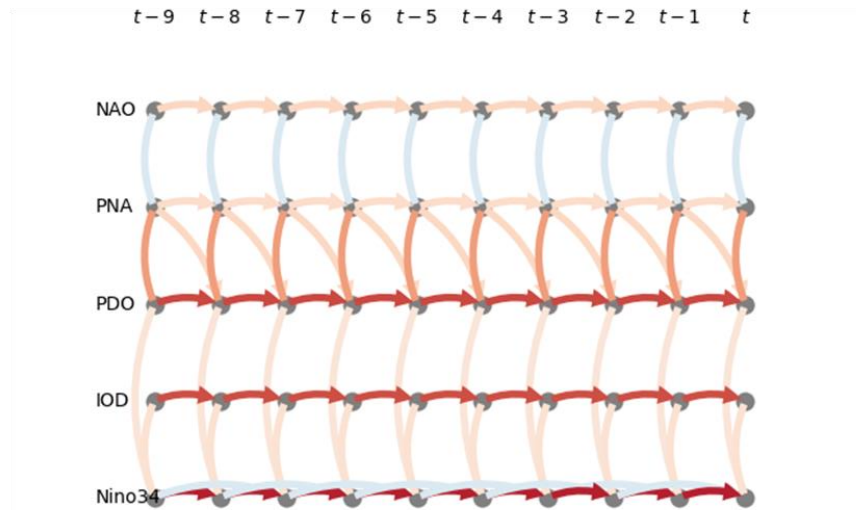
- YU, B. AND ZWIERS, F.W., 2007. THE IMPACT OF COMBINED ENSO AND PDO ON THE PNA CLIMATE: A 1,000-YEAR CLIMATE MODELING STUDY. CLIMATE DYNAMICS, 29(7): 837-851.
- ZHANG, Y., XIE, S.-P., KOSAKA, Y. AND YANG, J.-C., 2018. PACIFIC DECADAL OSCILLATION: TROPICAL PACIFIC FORCING VERSUS INTERNAL VARIABILITY. JOURNAL OF CLIMATE, 31(20): 8265-8279.
- ZHENG, X.-T., XIE, S.-P., DU, Y., LIU, L., HUANG, G. AND LIU, Q., 2013. INDIAN OCEAN DIPOLE RESPONSE TO GLOBAL WARMING IN THE CMIP5 MULTIMODEL ENSEMBLE. JOURNAL OF CLIMATE, 26(16): 6067-6080.

9. APPENDIX



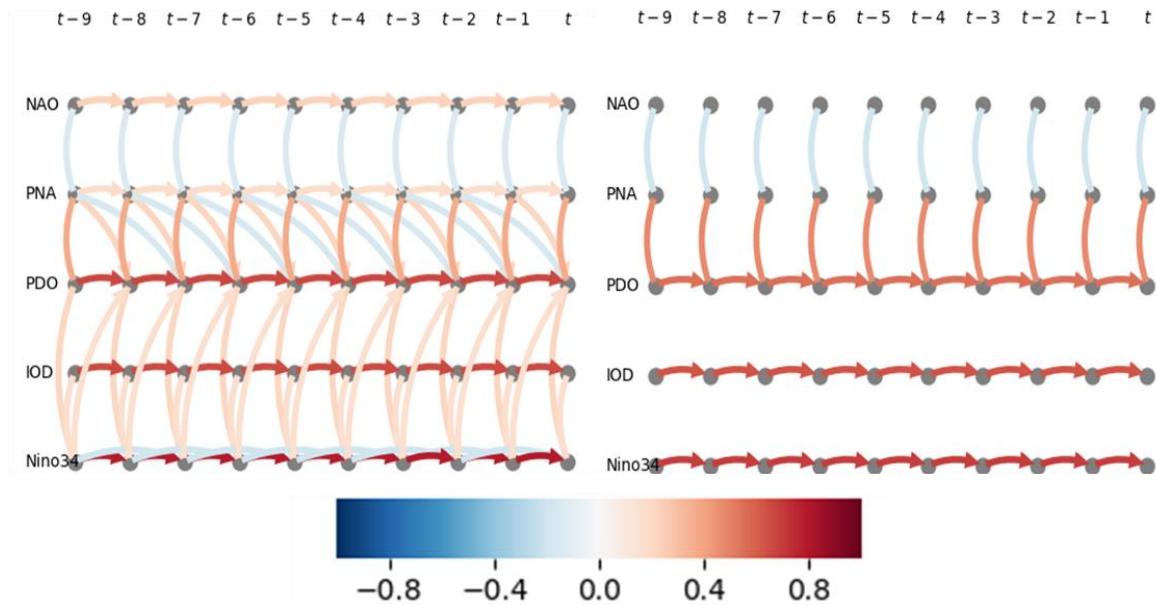
Appendix 1. Process graphs for models and reference dataset. No filter applied. Plots produced by Ti-gramite

No Mask applied



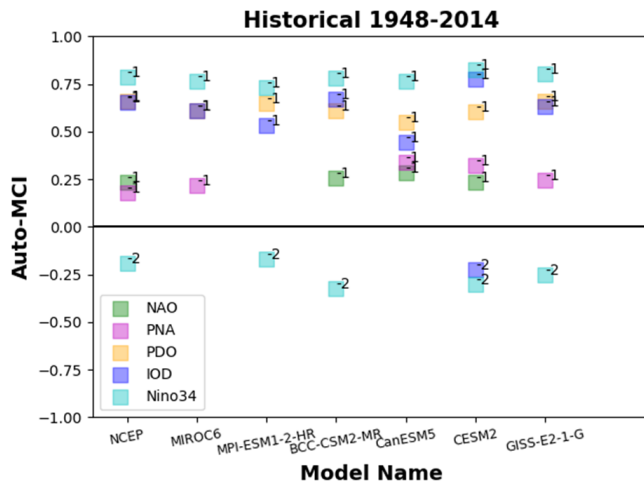
PDO/ENSO in phase

PDO/ENSO out of phase

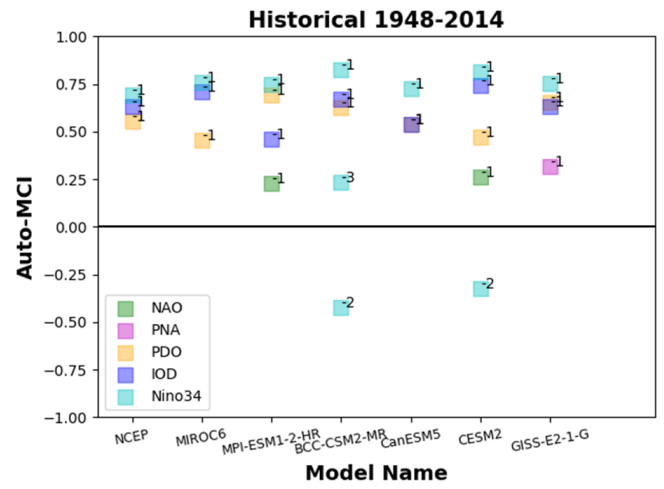


Appendix 2. Time series graph is better for the understanding of the spatio-temporal framework of the dependency structure through the displayed causal pathways. Negative auto-correlations can be seen here (as blue arrows) connecting different time steps of the same variable. Here, time series graph are for the historical non-filter data. Plots produced by Tigramite.

PDO/ENSO in phase

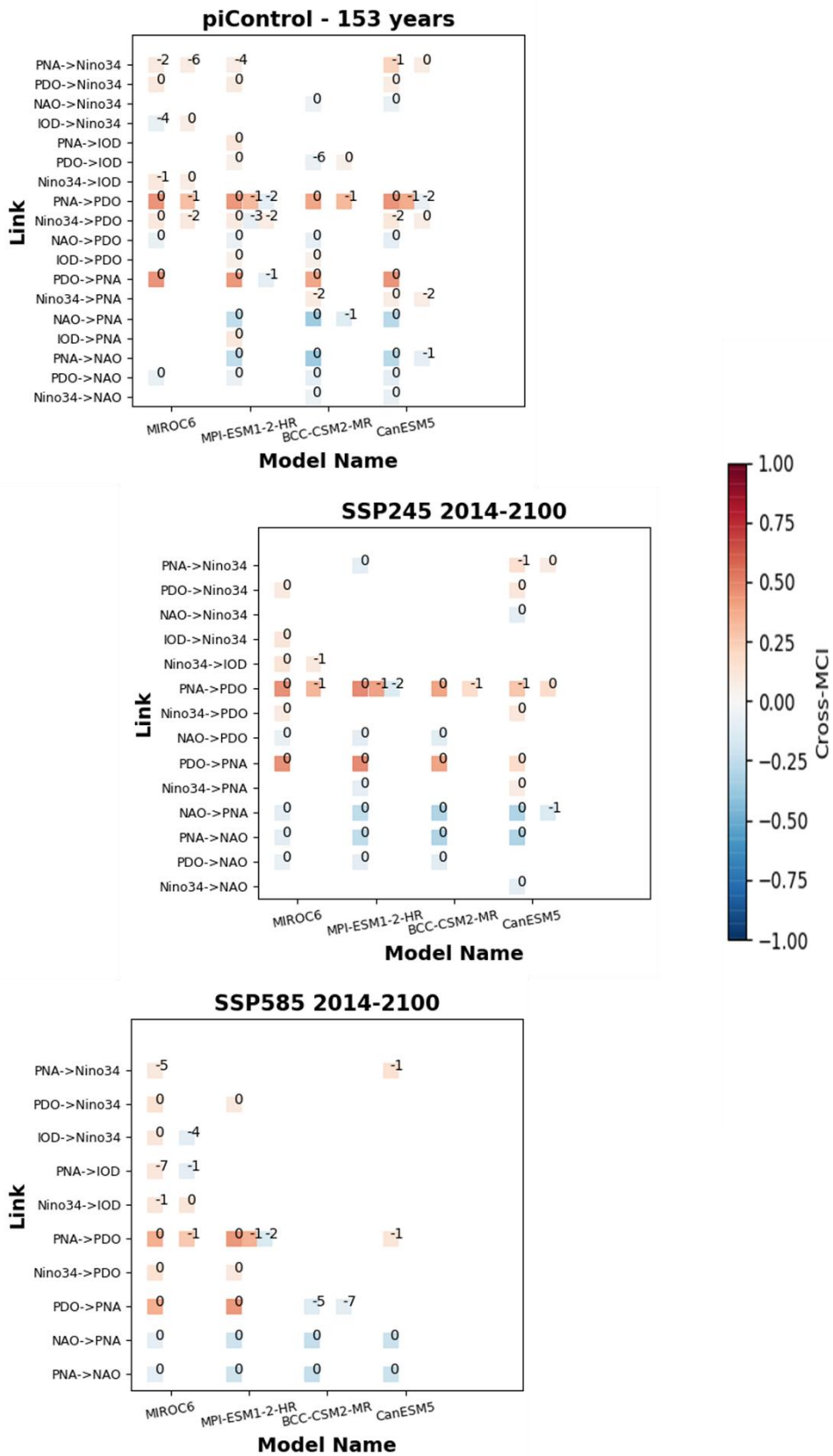


PDO/ENSO out of phase



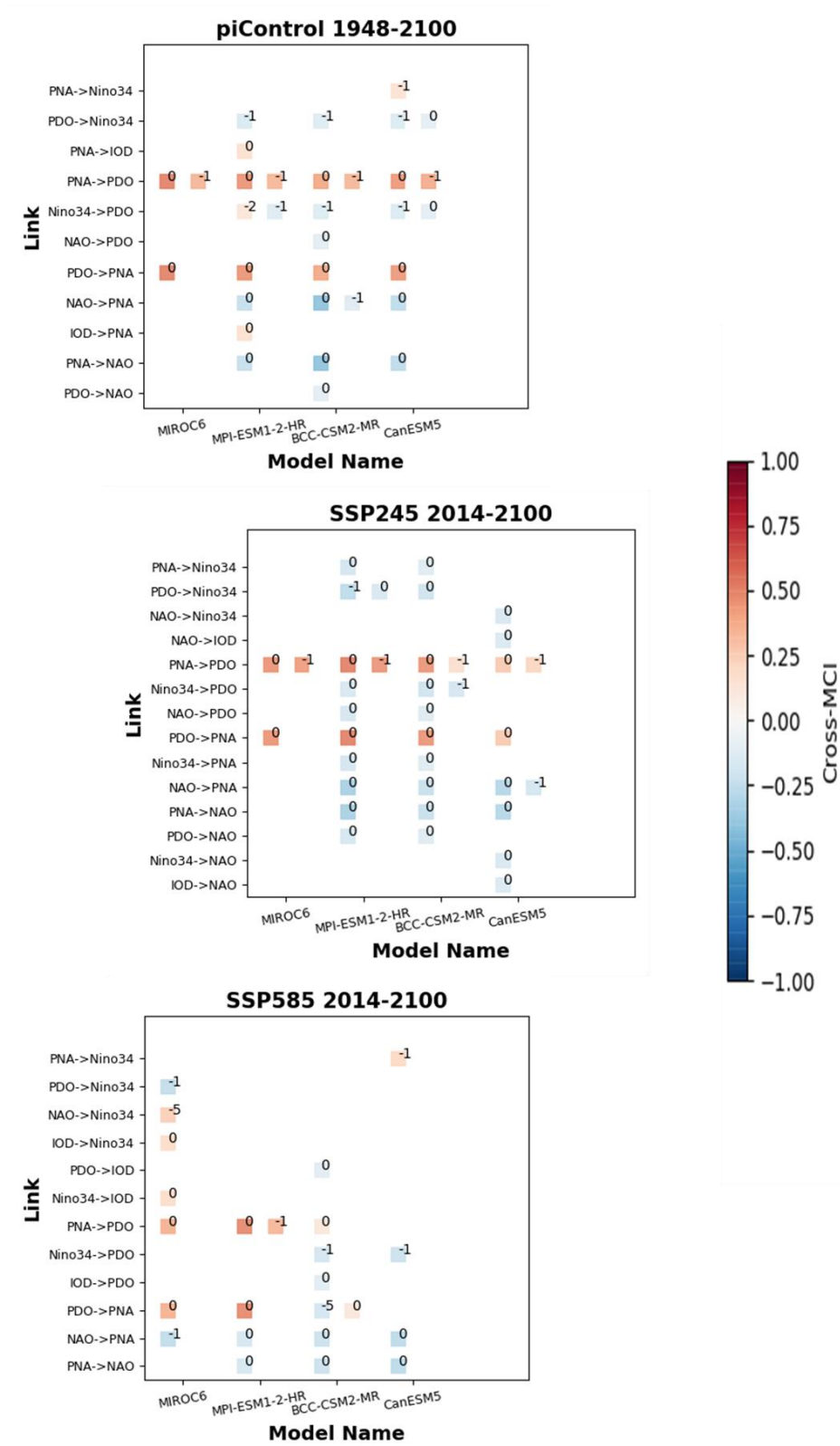
Appendix 3. Summary of auto-MCI values for the different indices are mainly consistent through NCEP and model data. Results from historical data (1948-2014)

No Mask applied



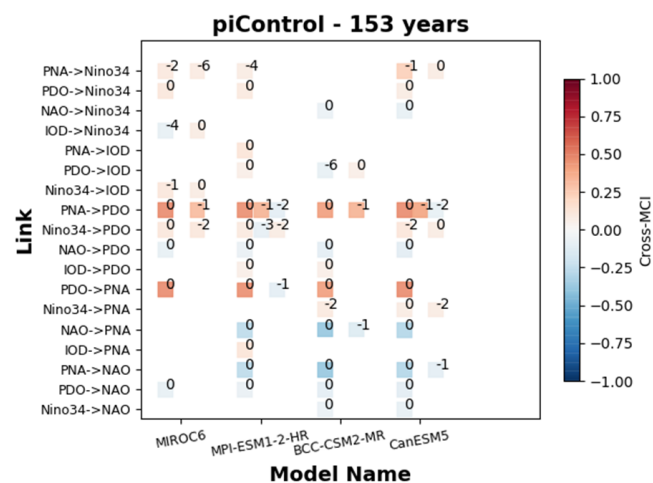
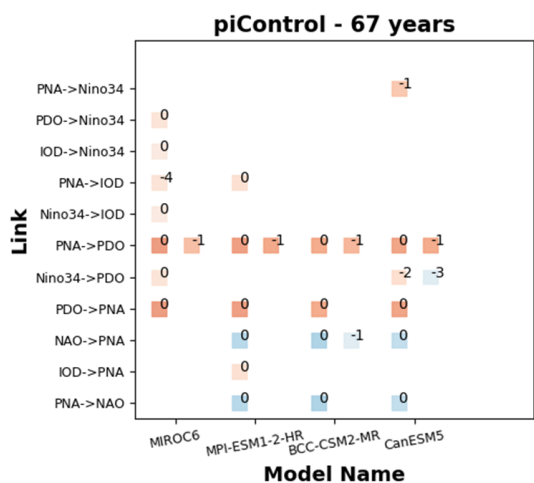
Appendix 4. Link summary plots for the unfiltered data using three simulations: piControl (top), SSP245 (middle), SSP585 (bottom)

PDO/ENSO out of phase



Appendix 5. Link summary plots for the out-of-phase regime using three simulations: piControl (top), SSP245 (middle), SSP585(bottom)

No Mask applied



Appendix 6. Link Summary plots for 67-year (left) and 153-year (right) piControl simulations using unmasked data.

LIST OF FIGURES

- FIGURE 1.** RANDOM ATMOSPHERIC HEAT FLUX FORCING TIME SERIES (TOP) AND THE UPPER-OCEAN MIXED-LAYER TEMPERATURE RESPONSE FOR A MIXED-LAYER DEPTH OF 50 M (MIDDLE) AND 500 M (GRAPH). (DESER ET AL., 2010) 9
- FIGURE 2.** SCHEMATIC DIAGRAMS SHOWING THE WEATHER AND OCEAN CONDITIONS ASSOCIATED WITH NORMAL CONDITIONS (TOP), EL NIÑO (MIDDLE), AND LA NIÑA (BOTTOM). FIGURE COURTESY OF THE NATIONAL OCEANIC AND ATMOSPHERIC ADMINISTRATION (NOAA). 12
- FIGURE 3.** SCHEMATIC OF THE TWO-STEP APPROACH DURING THE CAUSALITY ANALYSIS. PART A: THE PROCESS FOLLOWED TO PRODUCE THE TIME SERIES FOR VARIABLES AND INDICES USING THE CVDP IMPLEMENTED INSIDE THE ESMVALTOOL. PART B: CAUSALITY ANALYSIS USING PCMCI, TAKING AS INPUT THE TIME SERIES PRODUCED IN PART A. 20
- FIGURE 4.** SCHEMATIC OF THE CAUSAL DISCOVERY METHOD PCMCI. A) THE PC1 CONDITION SELECTION ALGORITHM FOR THE VARIABLES X1 (TOP) AND X3 (BOTTOM): BY ITERATIVELY REMOVING THE CONDITIONALLY INDEPENDENT VARIABLES, THE PC1 ALGORITHM CONVERGES TO A SMALL SET OF RELEVANT CONDITIONS (DARK RED/BLUE) WITH THE POTENTIAL PRESENCE OF SOME FALSE POSITIVES (BOXES WITH ASTERISK). B) THE OBTAINED LOW-DIMENSIONAL CONDITIONS ARE THEN USED DURING THE MCI. THE CONDITIONS, $\wp(Xt3)$ (PARENTS OF $Xt3$, BLUE BOXES) ARE SUFFICIENT TO ESTABLISH CONDITIONAL INDEPENDENCE FOR TESTING $Xt - 21 \rightarrow Xt3$. THE REMAINING CONDITIONS $\wp(Xt - 21)$ (RED BOXES) ARE USED TO ESTIMATE THE STRENGTH OF THE CAUSAL EFFECT. FIGURE COURTESY OF RUNGE ET AL. (2017)..... 22
- FIGURE 5.** PROCESS GRAPH AGGREGATING INFORMATION OF CAUSAL EFFECT OF SURFACE AIR TEMPERATURE (TAS) ANOMALIES BETWEEN WEUR AND EEUR. NODE COLOUR, REPRESENTING THE AUTO-MCI VALUE, DENOTES THE MAXIMUM ABSOLUTE AUTO-DEPENDENCY. THE LINK COLOUR REPRESENTS CROSS-MCI VALUE, AND LINK LABEL THE TIME LAG (IN MONTHS). THIS RESULT IS PRODUCED USING TIGRAMITE FOR THE REFERENCE DATASET NCEP. 23
- FIGURE 6.** SUMMARY OF LINK STRENGTHS (CROSS-MCI VALUES) ACCORDING THE DATASET USED. THE COLOUR OF THE BOXES DENOTES THE CROSS-MCI VALUE OF THE LINK. THE LABELS ON THE BOXES REFER TO THE TIME LAG FOR WHICH THE TELECONNECTION IS FOUND TO BE EFFECTIVE. MIROC6 AND MRI-ESM2-0 DO NOT PRODUCE ANY LINKS AT ALPHA=0.01. 24
- FIGURE 7.** PROCESS GRAPH AGGREGATING INFORMATION OF CAUSAL EFFECT OF SURFACE AIR TEMPERATURE (TAS) AND SURFACE PRESSURE (PSL) ANOMALIES OVER EPAC, CPAC AND WPAC. NODE COLOUR DENOTES AUTO-MCI VALUE, LINK COLOUR CROSS-MCI VALUE, AND LINK LABEL THE TIME LAG (IN MONTHS). WHEN A LINK HAS MORE THAN ONE TIME-LAG LABEL, THE LINK COLOUR DENOTES THE LINK WITH THE HIGHEST ABSOLUTE CROSS-MCI VALUE; TIME LAGS ARE SORTED ACCORDING TO THEIR $|\text{CROSS-MCI}|$. UNDIRECTED NON-CURVED LINKS DENOTE CONTEMPORANEOUS CONNECTIONS HAPPENING AT A TIME LAG $t < 1$ MONTH. THIS RESULT IS PRODUCED USING TIGRAMITE FOR THE REFERENCE DATASET NCEP (LEFT) AND THE MULTI-MODEL MEAN OF THE 5 CMIP6 MODELS (RIGHT)... 25
- FIGURE 8.** SUMMARY OF THE LINKS PRODUCED ACCORDING THE DATASET USED. A 0-MONTH TIME LAG DENOTES A CONTEMPORANEOUS UNDIRECTED LINK BETWEEN THE VARIABLES HAPPENING AT A TIME LAG SHORTER THAN 1 MONTH. THESE LINKS ARE SHOWN TWICE IN

THE FIGURE. NCEP IS THE ONLY DATASET TO NOT PRODUCE A POSITIVE LAGGED CPAC→WPAC CONNECTION (AT ALPHA=0.01).....	26
FIGURE 9. MATRIX OF LAG FUNCTIONS BETWEEN THE FIVE INDICES: NAO, PNA, PDO, IOD AND NINO34 (CONDITIONAL ON THE PAST OF ALL-TIME SERIES UP TO TMAX = 9 MONTHS). THIS RESULT IS PRODUCED USING TIGRAMITE	27
FIGURE 10. TIME SERIES FOR NAO, PNA, PDO, IOD AND NINO34 INDICES, COMPUTED BY CVDP USING THE NCEP REANALYSIS DATASET FOR THE 1948-2014 PERIOD (804 MONTHS). GREY SHADED AREA IS THE MASKED PERIOD OF THE TIME SERIES WHEN PDO AND ENSO ARE OUT OF PHASE. FIGURE PRODUCED BY TIGRAMITE.	28
FIGURE 11. PROCESS GRAPHS AGGREGATING THE CAUSAL EFFECT BETWEEN THE FIVE INDICES (MODES) FOR THE UNMASKED WHOLE TIME SERIES (TOP), THE IN-PHASE COMBINATION OF PDO AND NINO34 (BOTTOM LEFT) AND THE OUT-OF-PHASE COMBINATION OF PDO AND NINO34 (BOTTOM RIGHT). GRAPHS ARE PRODUCED BY TIGRAMITE FOR THE 1948-2014 PERIOD USING THE NCEP REANALYSIS DATASET.	29
FIGURE 12. SUMMARY PLOT FOR THE LINKS PRODUCED DURING A NON-FILTERED (NO MASK APPLIED) PCMCI RUN OF HISTORICAL DATA (1948-2014) USING NCEP AND DIFFERENT CMIP6 MODELS, NUMBERS DENOTE THE TIME LAG. NOTICE THAT CONTEMPORANEOUS UNDIRECTED LINKS (LAG=0) ARE DISPLAYED TWICE.....	30
FIGURE 13. SUMMARY OF AUTO-MCI VALUES FOR THE SAME RUN (AS FIGURE 12) DEPENDING ON THE DATASET USED. BOX COLOR DENOTES THE VARIABLE, BOX LABEL DENOTES THE LAG OF THE AUTO-CORRELATION.	30
FIGURE 14. THE SAME AS FIGURE 12 BUT FOR DIFFERENT REGIMES. TO THE LEFT ARE THE LINKS FOUND DURING THE PDO/ENSO IN-PHASE REGIME. THE PLOT ON THE RIGHT CONTAINS LINKS PRODUCED FOR THE PDO/ENSO OUT-OF-PHASE REGIME.	31
FIGURE 15. SUMMARY PLOT FOR THE LINKS PRODUCED DURING A PCMCI RUN FOR A PICONTROL RUN SIMULATING THE 1948-2100 (153 YEARS) PERIOD FOR THE PDO/ENSO IN-PHASE REGIME, NUMBERS DENOTE THE TIME LAG. NOTICE THAT CONTEMPORANEOUS UNDIRECTED LINKS (LAG=0) ARE DISPLAYED TWICE. RESULTS FOR 4 CMIP6 MODELS.	32
FIGURE 16. THE SAME AS FIGURE 15 BUT FOR SSP245 (LEFT) AND SSP585 (RIGHT) SIMULATING THE 2014-2100 (87 YEARS) PERIOD.	33
FIGURE 17. SUMMARY PLOTS FOR THE LINKS PRODUCED DURING A PCMCI RUN FOR HISTORICAL SIMULATION (LEFT) AND 153-YEAR PICONTROL SIMULATION (RIGHT). BOTH RESULTS WERE PRODUCED USING UNMASKED DATA.....	34

LIST OF TABLES

TABLE 1. CMIP6 MODELS, THEIR ATMOSPHERE AND OCEAN COMPONENTS, AND SIMULATIONS USED IN THIS ANALYSIS. HIGHLIGHTED ARE THE MODELS USED IN THE MAIN REGIME-ORIENTED ANALYSIS EXAMPLE (SEE SECTION 5.2).....	16
TABLE 2. DESCRIPTION OF INDICES USED DURING THE REGIME-ORIENTED ANALYSIS AS CALCULATED BY CVDP.	18